

Spectrum of slip dynamics, scaling & statistical laws emerge from simplified model of fault and damage zone architecture

M. Almakari^{1,†}, N. Kheirdast^{1,†}, C. Villafuerte^{1,*}, M. Y. Thomas², P. Dubernet¹, J. Cheng^{1,§}, A. Gupta¹, P. Romanet^{3,4}, S. Chaillat⁵, H. S. Bhat^{1,¶}

1. Laboratoire de Géologie, Ecole Normale Supérieure, CNRS-UMR 8538, PSL Research University, Paris, France
2. Université de Rennes, CNRS, Géosciences Rennes, CNRS-UMR 6118, Rennes
3. Department of Earth Sciences, La Sapienza University of Rome, Piazzale Aldo Moro 5, 00185 Roma, Italy
4. Université Côte d'Azur, CNRS, IRD, Observatoire de la Côte d'Azur, Géoazur, Sophia-Antipolis, 06560 Valbonne, France
5. Laboratoire POEMS, CNRS-INRIA-ENSTA Paris, Institut Polytechnique de Paris

† M. Almakari and N. Kheirdast contributed equally to this work.

* Currently at Instituto de Geofísica, Universidad Nacional Autónoma de México

§ Currently at Division of Geological and Planetary Sciences, California Institute of Technology.

¶ Corresponding author: harshasbhat@gmail.com

CRedit

Conceptualization:	H. S. Bhat
Methodology:	H. S. Bhat, M. Y. Thomas
Software:	H. S. Bhat, M. Almakari, N. Kheirdast, C. Villafuerte, P. Romanet, S. Chaillat
Investigation:	M. Almakari, N. Kheirdast, C. Villafuerte, H. S. Bhat, J. Cheng
Writing - original draft:	M. Almakari, N. Kheirdast
Writing - review & editing:	H. S. Bhat, N. Kheirdast, C. Villafuerte, M. Y. Thomas, J. Cheng, A. Gupta, P. Romanet, S. Chaillat
Supervision:	H. S. Bhat, M. Y. Thomas
Funding acquisition:	H. S. Bhat

Abstract

Seismological and geodetic observations of a fault zone reveal a wide range of slip dynamics, scaling, and statistical laws. However, the underlying physical mechanisms remain unclear. In this study, we show that incorporating an off-fault damage zone-characterized by distributed fractures surrounding a main fault-can reproduce many key features observed in seismic and geodetic data. We model a 2D shear fault zone in which off-fault cracks follow power-law size and density distributions, and are oriented either optimally or parallel to the main fault. All fractures follow the rate-and-state friction law with parameters chosen such that each can host slip instabilities. We do not introduce spatial heterogeneities in the frictional properties of the fault. Using quasi-dynamic boundary integral simulations accelerated by hierarchical matrices, we simulate slip dynamics of this system and analyze the events produced both on and off the main fault. Despite the spatially uniform frictional properties, we observe a natural continuum from slow to fast ruptures, as observed in nature. Our simulations reproduce the Omori law, the inverse Omori law, the Gutenberg-Richter scaling, and the moment-duration scaling. We also observe seismicity localizing toward the main fault when an event is about to nucleate on the main fault. During slow slip events, off-fault seismicity migrates in a pattern resembling a fluid

diffusion front, despite the absence of fluids in the model. We also show that tremors, Very Low Frequency Earthquakes (VLFs), Low Frequency Earthquakes (LFEs), Slow Slip Events (SSEs), and earthquakes (EQs) can all emerge naturally in the ‘digital twin’ framework.

Plain Language Summary

Earthquake faults show complex behavior that ranges from slow creeping movements to fast and destructive ruptures, but their origin is not very clear. We investigated whether including the network of smaller cracks around a main fault—called the “damage zone”—could explain these observations. We created computer models of fault systems that included both the main fault and the surrounding fracture networks. We found that the geometric arrangement of these fractures alone could produce the full spectrum of fault behaviors observed in nature. Our simulations successfully reproduced well-known earthquake patterns, including how aftershocks decay over time, the relationship between earthquake size and frequency, and how seismic activity appears to migrate along fault zones. All major types of fault slip—from barely detectable slow movements to regular earthquakes—emerged naturally from the same model. This research suggests that the complex network of small fractures surrounding major faults plays a crucial role in earthquake behavior. Understanding these damage zones could improve our ability to assess seismic hazards and better predict how fault systems will behave over time.

1 Introduction

In the brittle upper crust, fault zone displays a large variety of slip dynamics and moment release. Until the discovery of SSEs (*Hirose et al. 1999; Dragert et al. 2001*) and tremor (*Obara 2002*), faults were thought to either remain locked during the interseismic period or continually creep—the former leading to stick-slip-like release of stored strain energy (*Brace & Byerlee 1966*), the latter to continuous strain release (*Steinbrugge et al. 1960*). Modern seismological and geodetic observations have significantly advanced our understanding of fault slip behavior, revealing a continuum of deformation modes spanning from regular fast earthquakes to a diverse family of slow earthquakes and/or steady creep. Slow earthquakes includes “seismic” members such as low-frequency earthquakes (LFEs), tectonic tremor, and very low-frequency earthquakes (VLFs), as well as “geodetic” members—slow slip events (SSEs)—typically classified as short-term (days to weeks) or long-term (months to years) (*Nishikawa et al. 2023*). These phenomena are increasingly recognized as different manifestations of a shared underlying physical process (*Beroza & Ide 2011; Ide & Beroza 2023*). SSEs, characterized by the gradual release of tectonic stress, have been observed in numerous subduction zones, including Cascadia, Central Ecuador, Guerrero, Hikurangi, Northern Chile, and southwest Japan, as well as along continental plate boundaries such as the San Andreas fault system in California, North Anatolian fault system, Haiyuan fault (*Lowry et al. 2001; Dragert et al. 2001; Rogers & Dragert 2003; Douglas et al. 2005; Jolivet et al. 2013; Vallée et al. 2013; Ruiz et al. 2014; Rousset et al. 2016; Shelly 2017; Michel et al. 2019; Dal Zilio et al. 2020*). These events often co-occur with LFEs and tremor, forming Episodic Tremor and Slip (ETS) sequences, particularly

well documented in Cascadia and Nankai (Rogers & Dragert 2003; Michel *et al.* 2019). Since their discovery, observations and models have emphasized the potential role of SSEs in the earthquake cycle. Occurring near or within the seismogenic zone, SSEs are thought to influence the initiation or modulation of large earthquakes (Rogers & Dragert 2003; Segall & Bradley 2012; Obara & Kato 2016; Cruz-Atienza *et al.* 2021). Moreover, aseismic slip phenomena are not limited to traditionally aseismic regions. Increasingly, observations show that slow and fast slip events can coexist within the seismogenic zone itself (Schwartz & Rokosky 2007; Ito *et al.* 2013; Ruiz *et al.* 2014; Thomas *et al.* 2017). Aseismic slip has notably been observed prior to several major earthquakes, including the 2011 Tōhoku-Oki (Ito *et al.* 2013), 2014 Iquique (Ruiz *et al.* 2014), and 2017 Valparaíso earthquakes (Ruiz *et al.* 2017; Caballero *et al.* 2021). Postseismic aseismic slip in seismic patches has also been documented in several subduction/collision zones (Johnson *et al.* 2012; Thomas *et al.* 2017; Villafuerte *et al.* 2025), further highlighting the complex interaction between seismic and aseismic processes.

Although slip dynamics may appear highly complex across timescales, robust empirical laws continue to emerge from seismological observations. The Gutenberg-Richter law describes the magnitude-frequency distribution of earthquakes, following a power law with a b -value near 1 (Gutenberg & Richter 1942). The Omori law characterizes the decay rate of aftershocks following a mainshock (Utsu *et al.* 1995), while an inverse Omori law describes the acceleration of foreshock activity before major events, first noted by Papazachos (1973). For fast ruptures, seismic moment scales cubically with rupture duration (Ide *et al.* 2008; Ide & Beroza 2023). For slow ruptures, debate remains between a linear scaling (Ide *et al.* 2008) and a cubic one (Gomberg *et al.* 2016; Michel *et al.* 2019). More recently, Kato & Ben-Zion (2020) reported a phenomenon of localization followed by delocalization of deformation before and after major earthquakes, respectively—a pattern observed in southern California for several large events, including the 1992 M_w 7.3 Landers, 1999 M_w 7.1 Hector Mine, and 2019 M_w 7.1 Ridgecrest earthquakes (Ben-Zion & Zaliapin 2020). Furthermore, seismicity has been observed to migrate during slow-slip events, with spatiotemporal features resembling a diffusion front, suggesting that fluid diffusion may govern these dynamics (for *e.g.* Danré *et al.* 2024).

The wide spectrum of observed slip behaviors has prompted investigation into various physical mechanisms, with fault friction heterogeneity emerging as the most commonly invoked (Brace & Byerlee 1966; Scholz 2019). Laboratory experiments have consistently shown that frictional properties are central to the transition from stable to unstable slip, particularly near the brittle-ductile transition zone (for *e.g.* Leeman *et al.* 2016; Tinti *et al.* 2016; Scuderi *et al.* 2016; Scuderi *et al.* 2017; Leeman *et al.* 2018; Siorattanakul 2024; Pignatelli *et al.* 2024; Yuan *et al.* 2024; Meyer *et al.* 2024; Salazar Vásquez *et al.* 2024). Numerical simulations incorporating variable constitutive friction parameters within rate-and-state frameworks have successfully reproduced a spectrum of slip modes, including slow ruptures (Yoshida & Kato 2003; Liu & Rice 2005; Barbot 2019; Nie & Barbot 2021). Modeling

and experimental studies indicate that frictional heterogeneity not only modulates slip dynamics and triggering (Aochi & Ide 2009; Dublanchet *et al.* 2013) but also governs complex precursory processes that may culminate in a mainshock (Kato *et al.* 1997; Ariyoshi *et al.* 2012; Dublanchet 2017; Gounon *et al.* 2022; Wang *et al.* 2023b). Other mechanisms have also been proposed, including fluid-related effects such as dilatant strengthening (Segall & Rice 1995; Segall *et al.* 2010; Liu & Rubin 2010), spatiotemporal variations in permeability and pore fluid pressure (Skarbek & Rempel 2016; Cruz-Atienza *et al.* 2018; Zhu *et al.* 2020; Perez-Silva *et al.* 2023; Ozawa *et al.* 2024), elastic or poroelastic bimaterial effects (Heimisson *et al.* 2019; Abdelmeguid & Elbanna 2022), brittle patches embedded in ductile matrices (Ando *et al.* 2012), and transient stress perturbations due to nearby earthquakes (Liu & Rice 2007) or failed nucleation processes (Rubin 2008). Notably, the earliest model of slow slip events was proposed by Perfettini *et al.* (2001), who showed that a spring-block system obeying rate-and-state friction and subjected to normal stress perturbations could, under certain conditions, exhibit “aseismic stick-slip” behavior—prior to the observational discovery of SSEs in Cascadia and the Bungo Channel.

However, faults are far more complex than simple, narrow shear zones idealized as frictional surfaces. Geological observations show that, surrounding the fine-grained fault core—where most slip localizes—is a broader damage zone composed of pervasively fractured rock with an intricate three-dimensional geometry across multiple length scales. (Sibson 1977; Chester *et al.* 1993; Biegel & Sammis 2004). This hierarchical geometric complexity ranges from tens of kilometers (*see, for e.g., Fletcher et al. 2014*) down to the millimetric scale (Sowers *et al.* 1994; Mitchell & Faulkner 2009; Fagereng *et al.* 2010). Figure 1 illustrates this hierarchical structure of fault systems over a wide range of length scales. Fault slip typically occurs on a localized plane—the fault core—which lies within a damage zone that generally extends several hundreds of meters in width (Chester & Logan 1986; Sibson 1986; Power *et al.* 1987; Ben-Zion & Sammis 2003; Sibson 2003; Savage & Brodsky 2011; Ostermeijer *et al.* 2020; Rodriguez Padilla *et al.* 2022; Liu *et al.* 2025). Various studies have shown that fault geometry—such as roughness (Candela *et al.* 2011; Cattania & Segall 2021; Ozawa & Ando 2021), bends (King & Nábělek 1985; Ritz *et al.* 2015; Romanet *et al.* 2020; Ozawa *et al.* 2023), branches (Aochi *et al.* 2000; Kame & Yamashita 2003; Kame *et al.* 2003; Oglesby 2003; Bhat 2004; Bhat *et al.* 2007b; Marschall & Douilly 2024), and step-overs (Oglesby 2005; Biasi & Wesnousky 2016; Rodriguez Padilla *et al.* 2024), play an important role in the dynamics of earthquake ruptures. Recent work has also underlined the key role of active faults networks (Im & Avouac 2023; Cheng *et al.* 2025). Large earthquakes ($M_w > 7$) often exhibit complex ruptures involving multiple faults (Stein & Bird 2024). For example, the 1992 Landers earthquake involved the activation of multiple faults during a single seismic event (Sowers *et al.* 1994; Fliss *et al.* 2005), and the 2016 Kaikōura earthquake involved at least 15 faults (Klinger *et al.* 2018). More recently, fault system geometry was found to significantly influence the slip distribution of the M_w 7.1 Ridgecrest earthquake (Nevitt *et al.* 2023) and the 2023 M_w 7.8 Kahramanmaraş, Turkey, earthquake (Chen

et al. 2024). Furthermore, recent work by *Lee et al. (2024)* suggests that fault slip stability may be controlled by the orientation and complexity of surrounding fault networks, with complex fault systems associated with locked segments that promote stick-slip behavior, whereas simpler geometries favor stable creep. Several studies have also focused on understanding the role of newly created fracture - or dynamic damage - in the propagation of a single dynamic rupture. This damage can significantly affect the high-frequency radiation generated during rupture propagation (*Thomas & Bhat 2018; Okubo et al. 2019; Marty et al. 2019; Okubo et al. 2020*). Recent findings highlight radiation from such multi-fracture structures in subduction zones (*Chalumeau et al. 2024*). Moreover, as a dynamic rupture propagates, the energy dissipated by off-fault frictional damage becomes critical to consider (*Okubo et al. 2019*). The fracture energy dissipated within the off-fault volume can be substantial—often comparable to the fracture energy on the main fault itself (*Andrews 2005; Okubo et al. 2019; Okubo et al. 2020*). Measurements of off-fault inelastic deformation using radar and optical imagery, when compared with aftershock sequences, indicate that fault systems exhibiting greater off-fault damage tend to produce relatively higher numbers of aftershocks (*Milliner et al. 2025*). Additionally, dynamic damage has been shown to play a crucial role in controlling the transition to supershear rupture (*Jara et al. 2021*).

Thus, while fault slip behavior is strongly influenced by the properties of the interface itself, the overall mechanical behavior of faults is equally shaped by the structural complexity of the entire fault zone. Its physical properties evolve over timescales ranging from seconds to millions of years, accommodating displacements from millimeters to tens of kilometers. In particular, dynamic ruptures can induce significant changes in both on-fault and off-fault microstructures and physicochemical properties. These changes, in turn, affects the style and dynamics of fault slip (*for e.g. Andrews 2005; Collettini et al. 2009; Niemeijer et al. 2010; Thomas et al. 2014; Faulkner et al. 2006; Dor et al. 2006b; Dor et al. 2006a; Mitchell & Faulkner 2009; Bhat et al. 2010; Okubo et al. 2019; Okubo et al. 2020*). Understanding such processes inevitably calls for a comprehensive approach that considers the fault zone as a whole, rather than focusing solely on the fault core.

Recent studies increasingly focus on understanding the role of complex and irregular geometries throughout the full seismic cycle. *Romanet et al. (2018)* incorporated geometrical complexity in numerical models and found that stress interactions between parallel faults can naturally generate slow slip events. Similarly, *Cattania & Segall (2021)* showed that foreshock sequences can emerge spontaneously when rough fault surfaces are considered. In a related study, *Ozawa & Ando (2021)* modeled a fault network with subsidiary fractures surrounding a primary rough fault and demonstrated the spontaneous emergence of an Omori-like aftershock decay (*Utsu et al. 1995*). Incorporating the realistic geometry of northern Cascadia into numerical models enabled the generation of slow slip events that closely match GPS observations in the region (*Li & Liu 2016*). Although an increasing number of studies explore the effects of geometry over multiple seismic

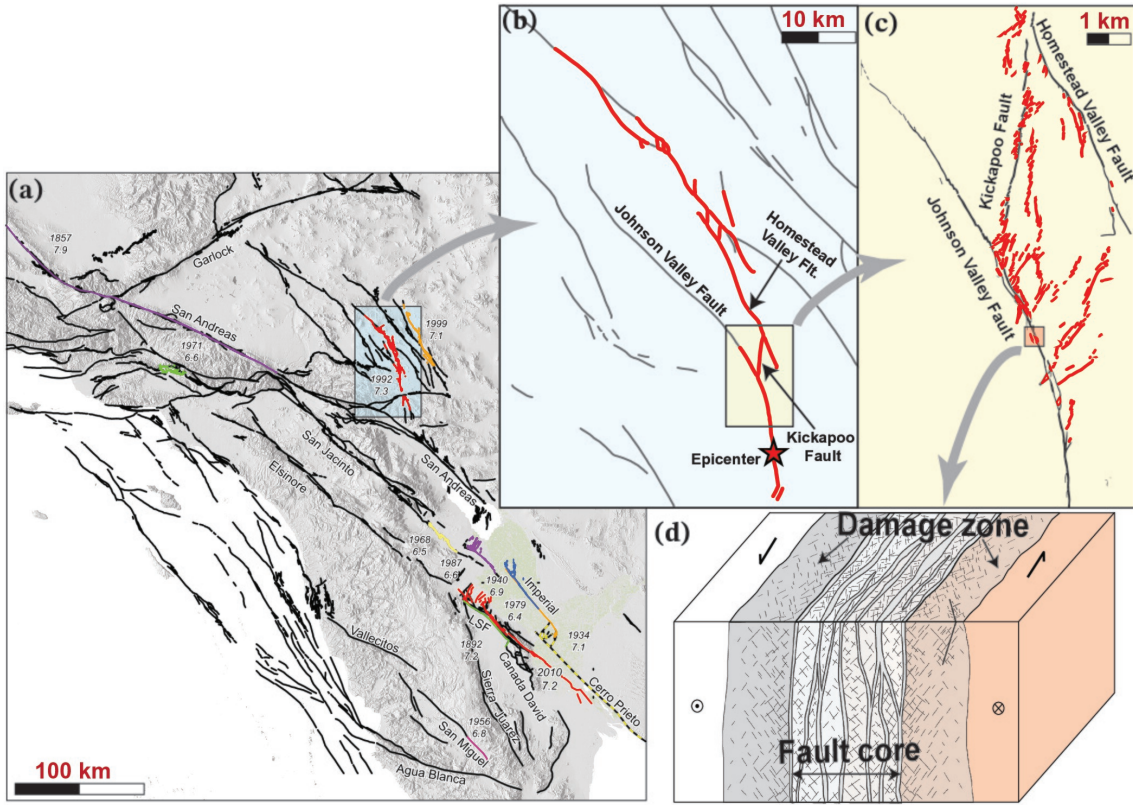


Figure 1: Hierarchical structure of fault systems over a wide range of length scales. (a) Fault map of Southern California (Fletcher *et al.* 2014). Black lines indicate fault traces. Stars and colored lines indicate the epicenters and rupture traces of historical earthquakes. (b) Fault map and rupture traces (in red) associated with the 1992 Landers earthquake (modified from Sowers *et al.* (1994)). (c) Smaller-scale off-fault fracture network (Sowers *et al.* 1994). (d) Schematic of fault zone structure, showing a fault core surrounded by damage zones (Mitchell & Faulkner 2009). Figure adapted from Okubo *et al.* (2019).

cycles, no current model reproduces the full range of observed slip dynamics (Yin *et al.* 2023; Im & Avouac 2024).

In this paper, we develop a fast and reliable model of quasi-dynamic earthquake cycles capable of incorporating complex fault geometries and networks under a rate-and-state friction law. Our approach is accelerated using hierarchical matrices, enabling the simulation of large, complex systems within reasonable computational time (see Appendix A for more details). Our goal is to investigate the role of realistic fault geometry (called fault volume henceforth) in the dynamics of slip events (at the scale of Figure 1d). We propose a simplified model of a 2D fault volume consisting of a main self-similar rough fault surrounded by a hierarchy of off-fault slip planes. All fractures are frictionally homogeneous (rate-weakening) and capable of dynamic slip. Remarkably, this purely geometric complexity is sufficient to reproduce the full spectrum of observed slip behaviors. The model can generate a continuum of slip events and recover all major empirical scaling laws associated with the seismic cycle.

In the following section, we introduce the fault volume model, stress loading, and initial conditions used in our study. We then outline the methodology for event detection, distinguishing between fast and slow ruptures, and describe our approach for constructing the synthetic earthquake catalog. In the results section, we begin with a case study illustrating the spatiotemporal evolution of seismic cycles and the emergence of complex slip dynamics. We then demonstrate the model's ability to reproduce key empirical laws, including the Gutenberg-Richter relation, moment-rupture area scaling, moment-duration scaling, and both Omori and inverse Omori laws. Additionally, we highlight the model's capacity to replicate the localization-delocalization transition of deformation. We further investigate the influence of fracture orientation and frictional behavior on seismic activity. Finally, we present a comprehensive synthetic catalog compiled from all simulations, offering insights into the statistical behavior of our fault volume model.

2 Fault Volume Model

This study focuses primarily on the impact of the geometry and architecture of fault zone on slip dynamics. Hence, this fault volume model is a simplified, canonical, representation of a fault and its damage zone. We begin by defining the elastic properties of the medium, its loading and initial conditions. All length scales are non-dimensionalized using frictional length scales (either the nucleation length or the cohesive zone size) computed using the initial stress state of the medium. These length scales are clearly approximations, as they evolve during the simulation as the the normal traction evolves due to loading and interaction. We then establish the frictional properties of the main fault and set its length to four times the nucleation length. Next, we define a damage zone with a width five times the cohesive zone size of the main fault. Within this damage zone, we assume a hierarchical distribution of off-fault fractures. The density of these fractures decreases according to a power law with fixed exponent and maximum value. The size distribution also follows a power law with a fixed exponent, where the smallest length scale is approximately 1m and the largest is on the order of the main fault length. We select the orientation distribution of these fractures from one of four possible configurations. We assume each off-fault fracture is twice its nucleation length to determine the critical slip distance, d_c , for each fracture. This ensures d_c scales automatically with fault length as described above. Finally, we statistically sample five times from the distributions (length, orientation, and density) to generate five samples of the fault volume model for a given orientation of the off-fault fractures and a/b ratio. We thus generate a total of 40 different fault volume models for this study each of them including around 700-1000 faults. In the following sections we describe each of the steps in more detail.

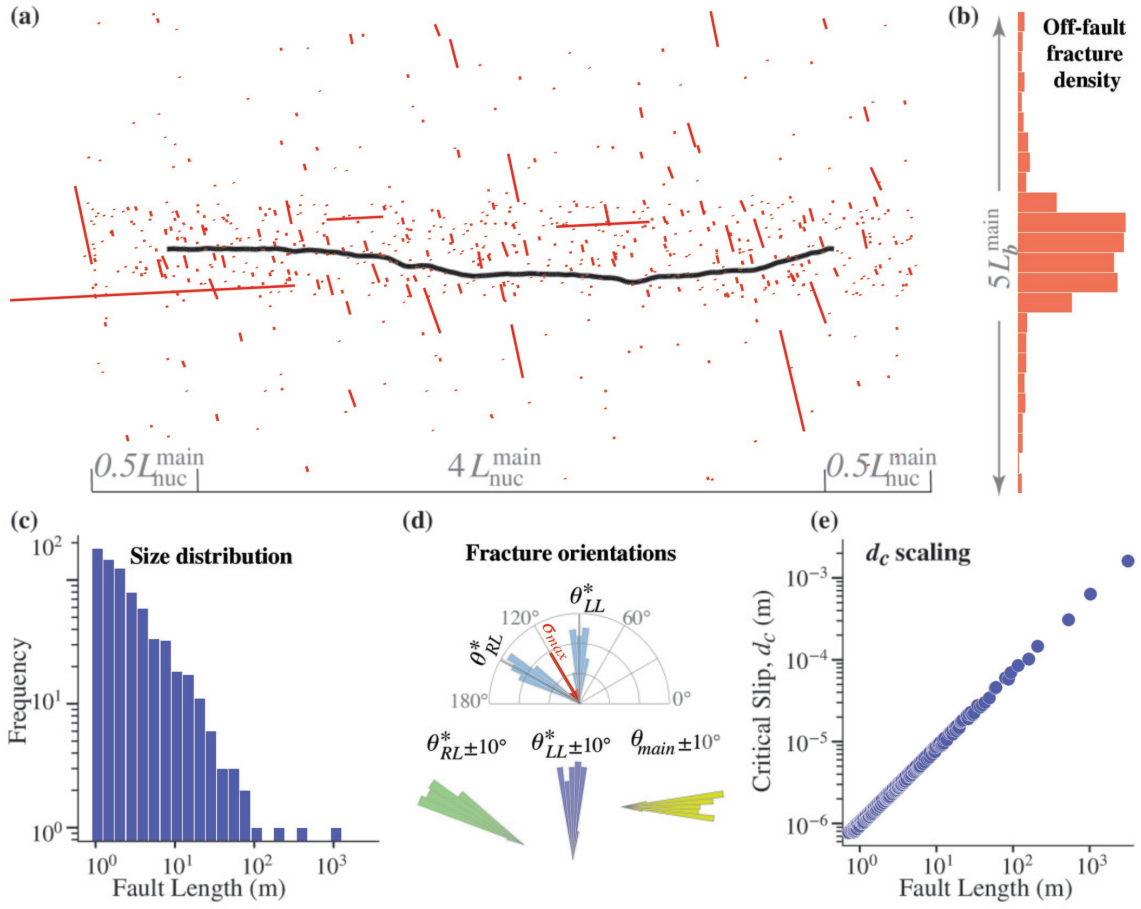


Figure 2: Fault volume geometry of a case study: a) sketch of fault volume geometry (not to scale): the main fault in black and the off-fault fractures in red b) off-fault fracture density perpendicular to the main fault (linear scale) c) probability density function of length distribution of the faults, including the main fault d) rose diagram of off-fault fracture orientations and principal stress direction e) critical slip distance of all fractures with respect to their length

2.1 Geometry of the main fault and its damage zone

The fault volume in the model comprises a main fault exhibiting right-lateral movement in an isotropic linear elastic medium ($\mu = 30$ GPa, $\nu = 0.25$), with fixed frictional properties, accompanied by off-fault fractures within a damage zone surrounding the main fault. Since geometric roughness is a characteristic observed at multiple scales in natural faults (Power *et al.* 1987; Schmittbuhl *et al.* 1993; Lee & Bruhn 1996; Renard *et al.* 2006; Candela *et al.* 2009; Candela *et al.* 2012), in this fault volume model, the main fault is characterized by self-similar roughness with $\alpha = 0.002$ (Dunham *et al.* 2011). Its extent is four times its nucleation length $L_{main} = 4L_{nuc}^{main}$ (Figure 2a). Note that the nucleation length is just an estimation, calculated for a single planar infinite fault, following Rubin & Ampuero (2005) and Viesca (2016) (See A8 for more details). We set the damage zone width as $W = 5L_b^{main}$ making it proportional to the main fault's cohesive zone size (L_b^{main}). This choice reflects the fact that the cohesive zone size governs the decay rate of stress perturbations from the main fault, which in turn controls the characteristic length scale over which main and

off-fault fractures interact (*Okubo et al. 2019*). We also add a fracture damage zone at each end of the main fault whose fracture density is assumed to be uniformly distributed.

From natural observations, the length distribution of off-fault fractures follows a power law (*Bonnet et al. 2001; Ben-Zion & Sammis 2003*). This modeling choice is grounded in the understanding that such distributions effectively capture the natural variability of fault lengths. Accordingly, we consider a power law distribution of fractures length with an exponent of 1 (Figure 2c). The smallest length scale is set to be around 1 m and the largest being of the order of the length of the main fault. Each off-fault fracture is set to be twice its nucleation length, ensuring it is large enough to rupture independently (*Rubin & Ampuero 2005; Viesca 2016*).

We next set the orientation statistics of the off-fault fractures. We experiment with four different orientations of fractures. In the first three cases, the fractures are deliberately well oriented to maximize reactivation and thus interaction with the main fault. We examine favorable orientations for right-lateral failure, left-lateral failure, and a combination of both (see example in Figure 2d). Optimal planes make an angle of $\theta = \pm (\pi/4 - 1/2 \tan^{-1} f_0)$ with the direction of maximum principal stress (*Bhat et al. 2007a*), where f_0 is the reference friction coefficient. Here $f_0 = 0.6$, so $\theta \approx \pm 30^\circ$. The initial maximum principal stress makes an angle of 120° with the horizontal axis. In this study, we will consider off-fault orientation distributions in the ranges $[90^\circ \pm 10^\circ]$ and $[150^\circ \pm 10^\circ]$, respectively. For the final case, the fractures run parallel to the main fault, as it has been observed that the growth process of faults reveals that off-fault cracks tend to be oblique by $[0^\circ - 20^\circ]$ to the trace of major faults (*Perrin et al. 2015*). For this case, we consider the fracture orientations in the range $[0^\circ \pm 10^\circ]$.

Observations from fault zones consistently show a significant decrease in the density of off-fault cracks with increasing distance from the main fault. This observation has been well documented in fault zones (*Chester & Logan 1986; Faulkner et al. 2006; Powers & Jordan 2010; Rodriguez Padilla et al. 2022*). Based on these observations of damage zones surrounding major faults, we model a power-law decay of fracture density with distance normal to the main fault, using an exponent of 1 (Figure 2b). We fix the peak density of off-fault fractures to be around 4 fractures per square meter, which is consistent with observations (*Chester & Logan 1986; Mitchell & Faulkner 2009; Faulkner et al. 2011; Rodriguez Padilla et al. 2022*). We further assume that all of the off-fault fractures are pure mode II fractures. The main numerical bottleneck in simulating tensile off-fault fractures in an earthquake cycle model is the lack of a good cohesive law that allows for the healing of the cohesive strength after rupture. We therefore restrict ourselves to shear fractures that follow rate-and-state friction law.

2.2 Frictional Parameters

Friction is assumed to follow regularized rate-and-state friction, spatially uniform and rate-weakening on all faults with $f_0 = 0.6$ (See A2). Specifically, for the main fault, the ratio a/b is fixed at 0.75 and d_c is set at 2 mm. Here, a is the direct effect parameter that governs the instantaneous change in friction with a change in slip rate, b is the evolution effect parameter which controls how friction evolves over time via changes in the state variable slip and d_c is the critical slip distance. Since a/b is a crucial parameter in controlling the frictional length scales (see A8) we parametrize the problem by varying this parameter. All off-fault fractures within the model share the same a/b ratio, with tested values of 0.4 and 0.5. The characteristic slip distance (d_c) is scaled with the length of off-fault fractures (Figure 2e) such that each off-fault fracture is twice the nucleation length.

Earthquake sources are conventionally modeled as shear ruptures occurring on preexisting faults within the seismogenic zone. Nevertheless, these faults are characterized by complex geometric irregularities and mechanical heterogeneities that manifest across a wide range of spatial scales throughout the fault zone. Be it in the lab scale or the field scale, the net weakening distance is a homogenized manifestation of weakening processes occurring at smaller scales (Ohnaka & Shen 1999; Gabriel et al. 2024). This approach is also inspired based on the observation that the so called fracture energy (G') scales with slip (Ohnaka 2003; Abercrombie & Rice 2005), and slip is itself related to fracture length, through elasticity. Furthermore, Rubin & Ampuero (2005) showed that fracture energy is approximately proportional to d_c within the rate-and-state friction framework. These observations together justify scaling d_c with fracture length in our model. This also has the additional advantage of keeping the computational cost reasonable. To keep the values of d_c realistic, we ensure that the smallest fracture is around 1 m, the length scale of laboratory experiments and use laboratory inferred values of d_c (Marone 1998; Scuderi et al. 2016; Leeman et al. 2018) of the order of several tens of microns.

2.3 Loading and Initial conditions

The medium has an initial prestress state with $\sigma_{11}^0 = -6.46$ MPa, $\sigma_{12}^0 = 3.88$ MPa, $\sigma_{22}^0 = -10.94$ MPa. It is also loaded with uniform far-field stressing rate, $\dot{\sigma}_{11}^\infty = -0.0064$ Pa s⁻¹, $\dot{\sigma}_{12}^\infty = 0.0038$ Pa s⁻¹, $\dot{\sigma}_{22}^\infty = -0.0108$ Pa s⁻¹. This corresponds to strain rates $\dot{\epsilon}_{11}^\infty = -4.93 \times 10^{-14}$ s⁻¹, $\dot{\epsilon}_{22}^\infty = -1.23 \times 10^{-13}$ s⁻¹ and $\dot{\epsilon}_{12}^\infty = 6.33 \times 10^{-14}$ s⁻¹. The direction of principal stress for far-field stress rate and initial stress are the same, and is assumed here to make an angle of 120° with the horizontal axis. At each fault, $\tau_0 = \sigma_{ij}^0 n_j s_i$ and $\sigma_0 = \sigma_{ij}^0 n_j n_i$, where τ_0 and σ_0 are initial shear and normal stress on the fault, n and s are the unit normal and unit tangent vectors respectively. All faults are assumed to be initially at steady state, and initial slip rates considered constant: $V_{\text{init}} = V_0 = 10^{-9}$ m/s where V_0 is the reference

slip rate for rate-and-state friction. The system initiates through the activation of a high slip rate patch located on the main fault. We neglect the first artificial earthquake on the main fault forced by loading, and only study the subsequent cycles after the system loses the memory of the initial conditions. To avoid unusual buildup of normal traction on the fault, we simply cap the normal stress at 10 MPa in an elastic-rigidly plastic sense. This needs to be examined in more detail in future work as it is beyond the scope of this paper. The slip rate is capped at a minimum value of 10^{-20} m/s at the end of each time step to avoid unnecessary numerical artifacts as suggested in the SEAS benchmark (*Jiang et al. 2022*).

2.4 Numerical Implementation

We implement the fault volume model using a quasi-dynamic boundary integral method with spatial convolution accelerated using hierarchical matrices. We account for the full elastic interaction between all faults in the system, including the main fault and all off-fault fractures. To ensure numerical accuracy, we discretize each of the faults such that at least 5 grid points are within the cohesive zone of each fault. This results in about 30000-50000 unknowns in the system per simulation. Each of the simulations is run until we produce between 8 and 10 major earthquakes on the main fault, which corresponds to between 2 and 4 million adaptive time steps. More details on the numerical implementation can be found in [Appendix A](#).

2.5 Event Detection and Catalog Generation

The detection and classification of events in the system involve several steps. Events are identified when the maximum slip rate exceeds predefined thresholds, with categorization into “fast” or “slow” depending on the specific threshold exceeded: 10^{-3} m/s for fast and 10^{-6} m/s for slow. Additional values for the slow rupture threshold (10^{-7} , 10^{-8} , and 10^{-9} m/s) are also tested. The effect of this threshold on the catalog and the scaling laws will be discussed in the following sections. Subsequently, events that fall within this threshold range are delineated spatiotemporally through the application of the connected-component labeling (CCL) algorithm, commonly utilized in image processing. The detailed event detection algorithm is presented in [Appendix B](#). This process yields information on rupture length L_{rup} and duration T , which allows us to estimate an average rupture velocity $v_r = L_{\text{rup}}/T$. We also estimate for each event the final slip δ and subsequently the seismic moment as follows: $M_0 = \mu S \delta$, where μ is the shear modulus and S is the rupture area. Since the model is 2D, we use an equivalent rupture surface S defined as $\pi L_{\text{rup}}^2/4$, assuming a circular rupture. We then estimate the moment magnitude $M_w = 0.67 \log_{10} M_0 - 6.06$ (*Hanks & Kanamori 1979*). Finally, we apply a filtering process to the detected events, eliminating those with fewer than 5 time steps and

spanning less than 5 grid points.

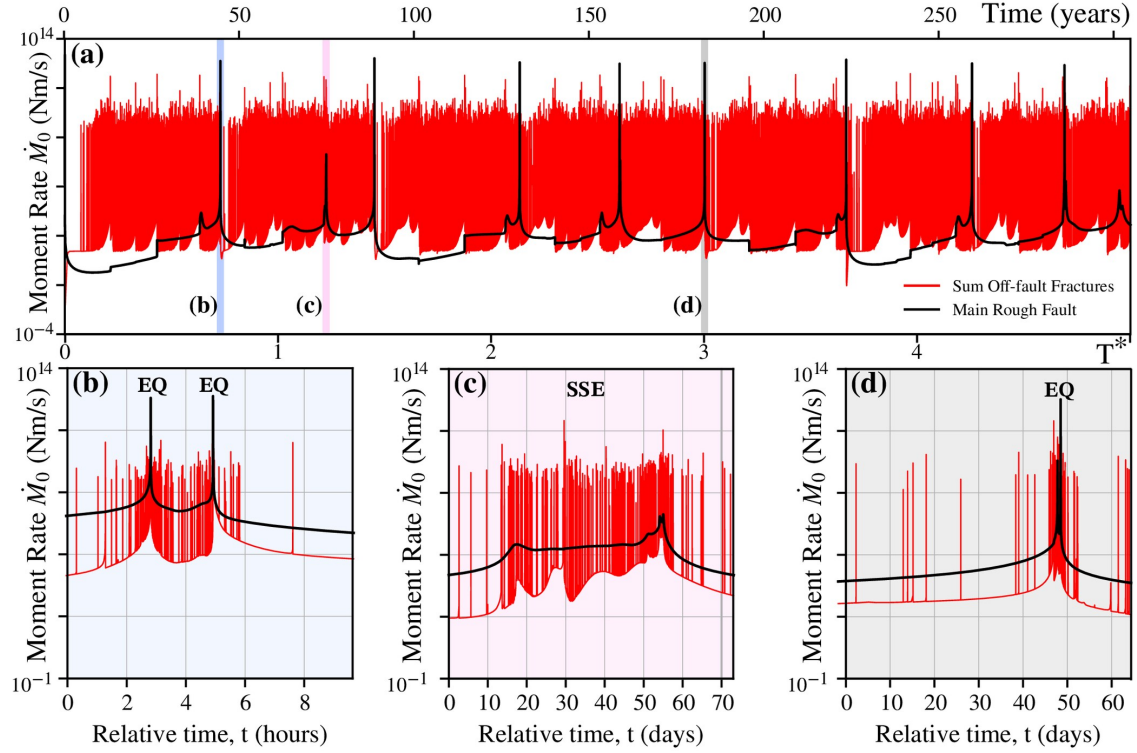


Figure 3: Time series of the moment rate \dot{M}_0 . The black curve represents the contribution coming from the main rough fault, and the red curve represents the summation of the moment rate released by all the fractures. Panel a) The entire seismic cycle. Top x-axis is absolute time in years, and bottom x-axis is time normalized by recurrence time of earthquakes when considering only the main rough fault, without a damage zone (~ 62 years). Panel b), c) and d) show time snapshots of the seismic cycle to highlight certain events. Here x-axis is relative time for the corresponding time snapshot. The spatiotemporal description of these events are shown in Figure 4.

3 Influence of the Fault Volume on the Slip Dynamics of the System

3.1 Seismic Cycles and Slip Dynamics

In this section, we provide a concise summary of results based on a case study. The geometric details are visually presented in Figure 2.

Figure 3 depicts the time series of the seismic moment rate released (\dot{M}_0), with the black curve illustrating the contribution originating from the main rough fault. In contrast, the red curve represents the cumulative moment rate released by all the off-fault fractures combined. In Figure 3a, in order to measure the impact of the fault volume on slip dynamics, we normalize time by recurrence time of earthquakes when considering only a single rough fault, without a damage zone. Notably, the presence of the fault volume introduces a higher frequency of ruptures on the main fault, revealing a significant increase

in seismic activity. Specifically, for the fault volume scenario presented here, we observe eight ruptures, twice as many as in the single-fault case, which exhibits only four over the same time period (Figure 3a). This substantial difference emphasizes the significant perturbation introduced by the fault volume on the seismic behavior of the system, resulting in a discernibly shorter recurrence interval. Importantly, the recurrence time is not constant but rather exhibits variability, giving rise to intricate seismic events. On the other hand, while the main fault experiences seismic cycles, we can observe that the off-fault fractures seem to be consistently releasing moment throughout the seismic cycle.

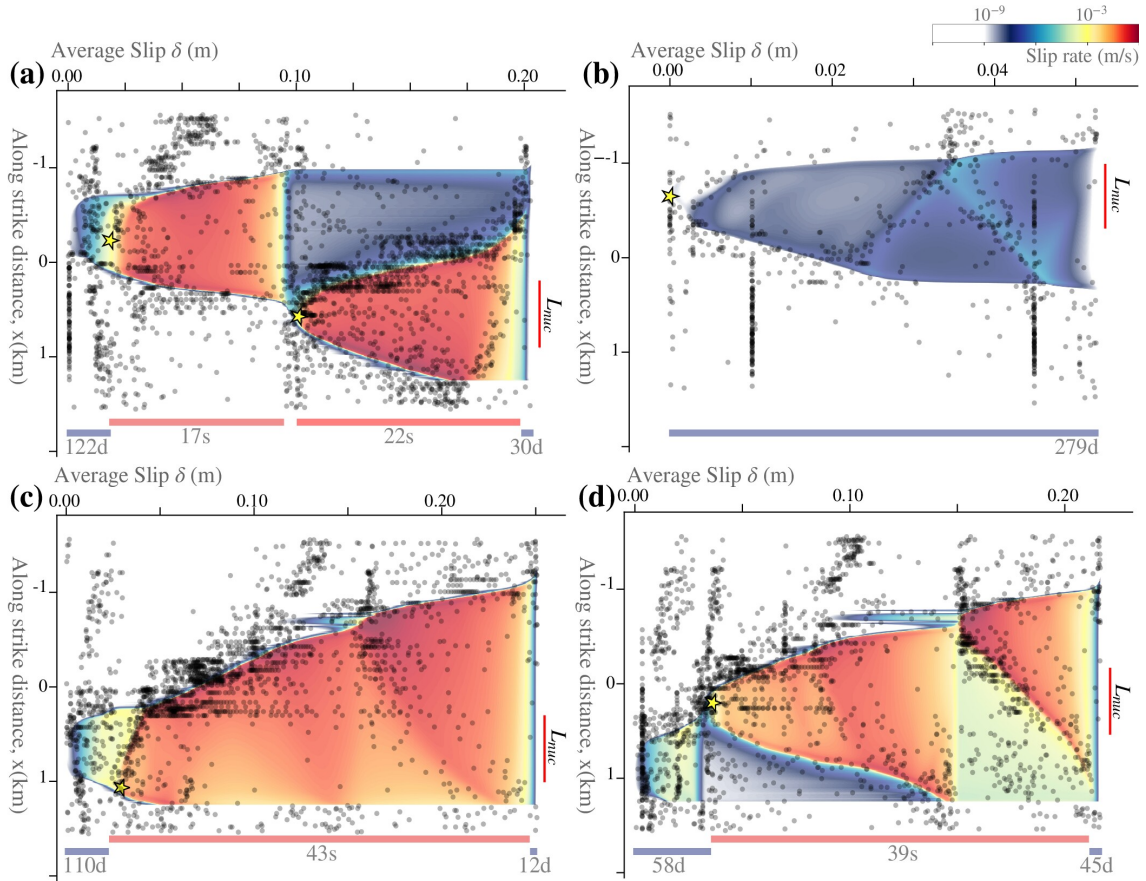


Figure 4: Sequences of slip rate profiles on the main fault. Top x-axis is average slip accumulated during the specific time sequence. Left y-axis represents the along-strike distance on the main fault. Horizontal lines show the specific durations for different phases of the rupture sequence, with blue lines indicating slow phases and red lines indicating fast phases. Nucleation and after-slip phases are indicated by two blue lines at the beginning and end of fast events. The colormap represents slip rate. Black circles represent events detected on the fractures, and projected onto the main fault strike. Yellow stars represent the epicenters of the different events. Panel a) shows complex partial ruptures on the main fault. Panel b) show one slow slip event. Panel c) shows a full rupture on the main fault. Panel d) shows an event, nucleated from one end of the fault and accelerated in a cascading process.

We observe both slow and fast earthquakes on the main fault, in comparison to the dynamics of a single main fault where only fast ruptures are observed. Figures 3b–d shed light on the complex seismic behavior driven by the presence of a fault volume. Examples include instances of multiple ruptures occurring within a brief timeframe, with intervals

as short as a few hours between them (Figure 3b). Additionally, we observe an increase in seismic activity recorded on the fractures before the rupture and a subsequent decrease afterward. This will be further discussed in the following sections. Furthermore, Figure 3c reveals the occurrence of prolonged slow slip events spanning a couple of months. These findings collectively underscore the complex nature of seismic activity influenced by the presence of a fault volume.

Having explored the temporal slip dynamics, our focus will now shift to examining the spatial complexity of the seismic events recorded on the main fault (Figure 4). In the presented figure, we delve into the spatial complexity of seismic events recorded on the main fault by looking at the slip rate profiles along strike as a function of spatially averaged cumulative slip. In addition, we project all off-fault activity during this event onto the main fault and denote them by simple black circles. For our analysis, we carefully selected several representative events from the case study, encompassing a diverse range of slip occurrences. This includes partial ruptures, full ruptures, and slow slip events, each characterized by distinct magnitudes and durations. For the fast ruptures, we present both the nucleation phase, where the slip rate starts to accelerate from an arbitrarily small threshold, i.e. 10^{-9} m/s, prior to reaching some geodetically detectable threshold, i.e., 10^{-6} m/s, and the afterslip phase, where the slip rate decelerates below the same limit. Figure 4a features two partial ruptures, each encompassing around half of the main fault. Notably, the second rupture (moment magnitude $M_w = 4.70$) nucleates at the edge of the first one ($M_w = 4.56$), demonstrating a cascading effect. Despite the rapid rupture of coseismic phases, which are 17 and 22 seconds, respectively, the nucleation phase lasting 122 days and the afterslip phase taking place over 30 days are significantly slower.

In Figure 4b, one slow slip event is showcased, rupturing only part of the main fault. This slow slip event spans 279 days with a moment magnitude $M_w = 4.48$. It is essential to acknowledge the subjectivity in detecting slow events due to the slip rate threshold used (here defined by slip rates between 10^{-9} and 10^{-3} m/s). This threshold effect will be discussed later in the text. We observe continuous seismic activity on the off-fault fractures accompanying the slow event on the main fault, as previously seen in Figure 3c. Figure 4c unfolds a full rupture on the main fault with a moment magnitude of $M_w = 5.03$, revealing nuanced variations in slip rate acceleration and deceleration within the rupture and along the fault's strike. The nucleation and afterslip of this event are 110 and 12 days, respectively. Figure 4d features another full rupture on the main fault ($M_w = 4.95$), preceded by a nucleation phase that ruptures around one-third of the main fault over 58 days. The rupture accelerates from the left corner of the nucleation patch. Then, the full rupture on the main fault lasts for 39 seconds; after a 45-day afterslip phase, the slip rate falls below 10^{-9} m/s. The figure illustrates a distinct cluster of off-fault events following the rupture front on the main fault.

4 Properties of the events in the catalog

In this section, we present the results of our numerical models, demonstrating their ability to replicate observed empirical statistical relationships and scaling laws governing seismic activity. These empirical relationships include the Omori law for the decay in the rate of aftershocks, Gutenberg-Richter magnitude-frequency distribution, the inverse-Omori law for foreshock escalation, moment-area scaling, and moment-duration scaling. We posit that any reasonable ‘digital twin’ of a fault system should be able to reproduce these empirical laws in addition to the range of slip dynamics. Through this analysis, we plan to show that our fault volume model not only produces a diverse range of slip dynamics but also satisfies key empirical laws observed in natural seismicity.

4.1 Omori Law

In seismological studies, the Omori law characterizes the temporal decay of aftershock activity following a mainshock event. This empirical law, commonly known as the Omori law, describes how the rate of aftershocks decreases over time following a seismic event. Specifically, it states that the number of aftershocks decreases inversely with time after the mainshock, following a power-law decay as follows: $n(t) = k/(c + t)^p$ where p is a constant that describes the decay rate and typically falls in the range 0.8–1.2 in most cases (*Omori 1894; Utsu et al. 1995*). In Figure 5a, we visualize the aftershock activity decay using stacked sequences from multiple seismic cycles within a simulation. Each gray line represents the aftershock activity following a single major seismic event, while the blue line represents the stacked sequences, providing an aggregated view of the aftershock decay pattern. By fitting the stacked sequences to the Omori law, we find a compelling match with an exponent p of 0.92, indicating a consistent decay rate across the simulated seismic events.

4.2 Gutenberg-Richter Magnitude Frequency Distributions

Figure 5b illustrates the magnitude-frequency distribution of ruptures from one of the simulations in our study. The x-axis denotes the magnitude range, while the y-axis represents the frequency of occurrences. Different distributions are plotted for fast, slow, and all ruptures. The distribution follows the Gutenberg-Richter law, exhibiting a logarithmic relationship between magnitude and frequency. This distribution provides crucial insights into the relative occurrence rates of seismic events of varying magnitudes, offering valuable information for seismic hazard assessment and earthquake forecasting. We can observe that the fast ruptures dominate the catalog in this case. To estimate the b-value, we utilize the maximum likelihood method (*Aki 1965*), compensating for the binning error (*Marzocchi & Sandri 2009*). We note that $M_w = -2$ approximately serves

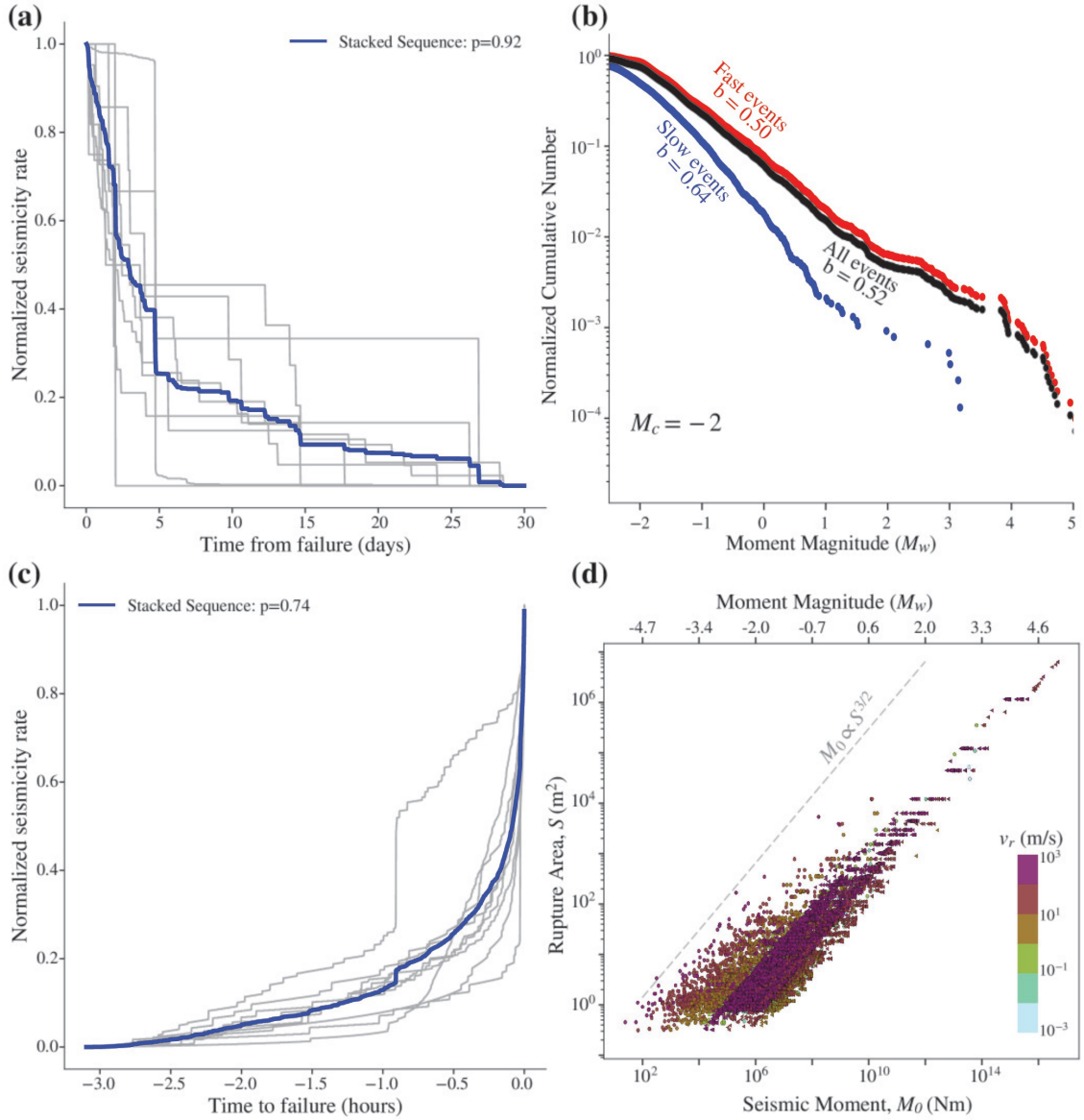


Figure 5: (a) Omori Law: Seismicity rate decreases over time following the mainshock. Each gray curve represents one earthquake cycle with one mainshock on the main fault, the blue curve represents the stacked sequences of all the seismic cycles in this simulation case (b) Magnitude-frequency distribution of the cataloged fast ruptures follows the Gutenberg-Richter distribution. Red and blue colors represent fast and slow ruptures respectively, while black color represents the total catalog (c) Inverse Omori: Seismicity rate increases inversely with time as the main rupture approaches. Each gray curve represents one earthquake cycle with one mainshock on the main fault, the blue curve represents the stacked sequences of all the seismic cycles in this simulation case (d) Scaling laws of inferred seismicity: Moment area scaling. Events are color-coded based on rupture velocity v_r .

as the completeness magnitude of our catalog. Our measured b -value for fast ruptures, approximately 0.5. As shown by *Aki (1981)*, a b -value between 0.5 and 1 can be envisaged when the fractal dimension is between 1 and 2 where the fault lines are distributed along a plane. This needs to be examined in much more detail. It is important to note that our primary objective is not to study the origin of the b -value derived from our fault

volume model. Rather, our focus is to demonstrate that considering the dynamics of a fault volume with fractures surrounding the main fault results in a logarithmic relationship between magnitude and frequency, consistent with the observed Gutenberg-Richter law in nature. While we suspect that the b -value may be influenced by factors such as the power-law distribution of fracture length and density distribution of fractures along fault-normal distance, we defer this exploration to future studies, as it falls beyond the scope of our current investigation.

4.3 Inverse Omori Law

In addition to the Omori-law-like reduction in the earthquake rate after a given event (section 4.1), the catalog of events in this paper’s simulation follows the empirical inverse Omori law that characterizes the increase in foreshock activity preceding a major rupture event. Unlike the aftershock decay described by the traditional Omori law, the inverse Omori law predicts a gradual rise in foreshock activity leading up to a significant seismic event, where foreshock rate increases as an inverse of the time to the mainshock as follows: $n(t) = 1/(c + \Delta t)^p$ (Jones & Molnar 1979; Shearer et al. 2023), where p is a constant that describes the increase rate of foreshocks and is typically around 1. In Figure 5c, we present the seismicity rate leading up to rupture events on the main fault, with each gray line representing the foreshock activity during a single seismic cycle. The blue line denotes the stacked sequences, providing an aggregated view of the precursor activity preceding significant ruptures. By fitting the stacked sequences to the inverse Omori law, we obtain a notable alignment with a parameter value of $p \approx 0.74$, close to 1. The alignment with the Omori law underscores its applicability in describing the temporal evolution of aftershock activity within our simulation. Similarly, the consistent trend of foreshock rate increase observed across our simulated seismic events aligns well with the predictive power of the inverse Omori law, demonstrating its ability to capture precursory behavior preceding major seismic events and laboratory earthquakes as shown in Marty et al. (2023).

4.4 Scaling Laws

Next, in Figure 5d, we explore the relationship between seismic moment (M_0) and rupture area (S) for both fast and slow ruptures. Notably, while determining rupture area (S) in nature can often be challenging, our model offers a straightforward approach as we have precise knowledge of fault behavior. Given our 2D model, we assume a circular rupture shape, simplifying the calculation of rupture area as equal to the square of rupture length. The figure reveals a scaling relation of $M_0 \propto S^{3/2}$, mirroring patterns observed in natural seismicity (Kanamori & Brodsky 2001). It is essential to note that this scaling law is consistent across both fast and slow ruptures.

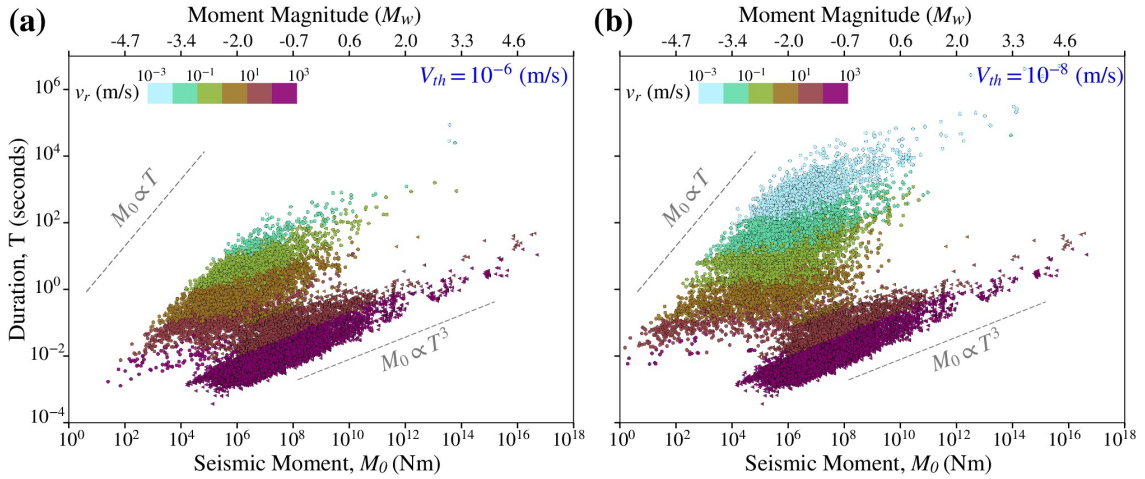


Figure 6: Scaling laws of inferred seismicity: Moment-duration scaling with a threshold of detection of slow ruptures at (a) 10^{-6} m/s and (b) 10^{-8} m/s. Events are color-coded based on rupture velocity v_r .

In Figure 6a, we delve into the moment-duration scaling, a crucial aspect of seismic rupture behavior. Observations in natural seismicity have highlighted a cubic relation between moment and duration for fast ruptures: $M_0 \propto T^3$ (Kanamori & Anderson 1975; Kanamori & Brodsky 2004; Houston 2001). However, for slow ruptures, the situation appears more complicated, with some observations suggesting a linear relation: $M_0 \propto T$ (Ide et al. 2007; Ide & Beroza 2023), while others indicating a cubic one (Gomberg et al. 2016; Michel et al. 2019). To investigate this further, we assess whether the detection threshold for slow ruptures influences the observed scaling relationship. Specifically, we examine Figure 6b, where the detection threshold is set to 10^{-8} m/s, and compare it to Figure 6a, which uses a threshold of 10^{-6} m/s. This comparison allows us to evaluate how the choice of detection threshold affects the apparent moment–duration scaling. Notably, the latter threshold is still three orders of magnitude smaller than the threshold for fast ruptures, set at 10^{-3} m/s. The color scale represents the logarithm of rupture velocity. The bottom x-axis displays seismic moment (M_0), while the top x-axis shows moment magnitude (M_w) for clarity and comparison with observational data. For the fast ruptures, we observe a clear cubic scaling ($M_0 \propto T^3$) between moment and duration, consistent with previous findings. However, the behavior of slow ruptures varies between the two figures. In Figure 6b with the lower detection threshold, we observe a linear relation between moment and duration. In contrast, Figure 6a with the higher threshold shows a trend closer to cubic scaling. This scaling is more apparent when we compile the entire catalog of all the simulations that we ran, and is displayed later in Figure 14. The effect of the detection threshold, ranging from 10^{-9} m/s to 10^{-6} m/s, on the detectable moment and magnitude of an example slow-slip rupture is shown in Figure 7a-d, highlighting how inferences drawn from the duration and moment of a slow-slip rupture could be changed if the lowest slip rate at which the rupture is initiated cannot be detected. This discrepancy suggests that the scaling between moment and duration for slow ruptures is

highly dependent on the detection threshold in our numerical model, akin to the sensitivity or threshold settings of field recording instruments or detection strategies employed on field data. In a recent work *Costantino et al. (2025)*, similar threshold-dependent effects were observed, in natural settings, when applying deep learning denoising techniques to reveal a continuum of slow slip events in the Cascadia subduction zone, demonstrating that detection methodology fundamentally shapes our understanding of slip behavior. Although the slip rate on the main fault may be very low and remain undetectable, the pattern of off-fault seismicity migration provides valuable information about the rupture process on the main fault, Figure 7e. The dot symbols on the plot represent off-fault events projected onto the main fault, marking the extents of the slow slip rupture. Further analysis is warranted to assess how reliably the pattern of off-fault seismic activity can be used to infer the magnitude and duration of a slow event, and we defer this investigation to future studies.

Since each of the events is color-coded based on its average rupture velocity in Figure 6, it is apparent that slow or fast events are identical in nature except for their rupture velocity. In fact, it is evident that $M_0 \propto T^3$ and $M_0 \propto T$ are limiting bounds in the moment-duration scaling as proposed by *Ide & Beroza (2023)*. This suggests that slow ruptures are simply fast ruptures with relatively lower slip rates, rupture velocities, and stress drops. This also implies that the slow ruptures do not emerge due to a special frictional constitutive law since it is the same mechanism that generates fast ruptures as well. What thus produces the difference in rupture velocity is the spatiotemporally complex traction on the main fault due to the presence of the fault volume.

4.5 Localization and Migration of Seismicity

In this section, we address the question of localization and delocalization of deformation throughout the seismic cycle, aiming to understand how deformation occurs in a fault volume over a seismic cycle. Over decadal timescales during the interseismic period, elevated background seismic activity may reflect progressive damage accumulation across a broad region that will eventually host a major earthquake. In several large events including the 1992 M_w 7.3 Landers, the 1999 M_w 7.1 Hector Mine, the 2019 M_w 7.1 Ridgecrest, and the 2023 M_w 7.8 Kahramanmaraş earthquakes, seismicity has been observed to migrate and concentrate toward the eventual rupture plane over a few years to several months preceding the mainshock. This localization appears to facilitate the interaction and coalescence of fault segments and fractures that delineate the future principal slip zone (*Ben-Zion & Zaliapin 2019; Ben-Zion & Zaliapin 2020; Pritchard et al. 2020; Kato & Ben-Zion 2020; Kwiatek et al. 2023; Núñez-Jara et al. 2025*).

In our simulations, we quantify this localization by looking at the location of off-fault events over time. To this end, we calculate the standard deviation of hypocentral dis-

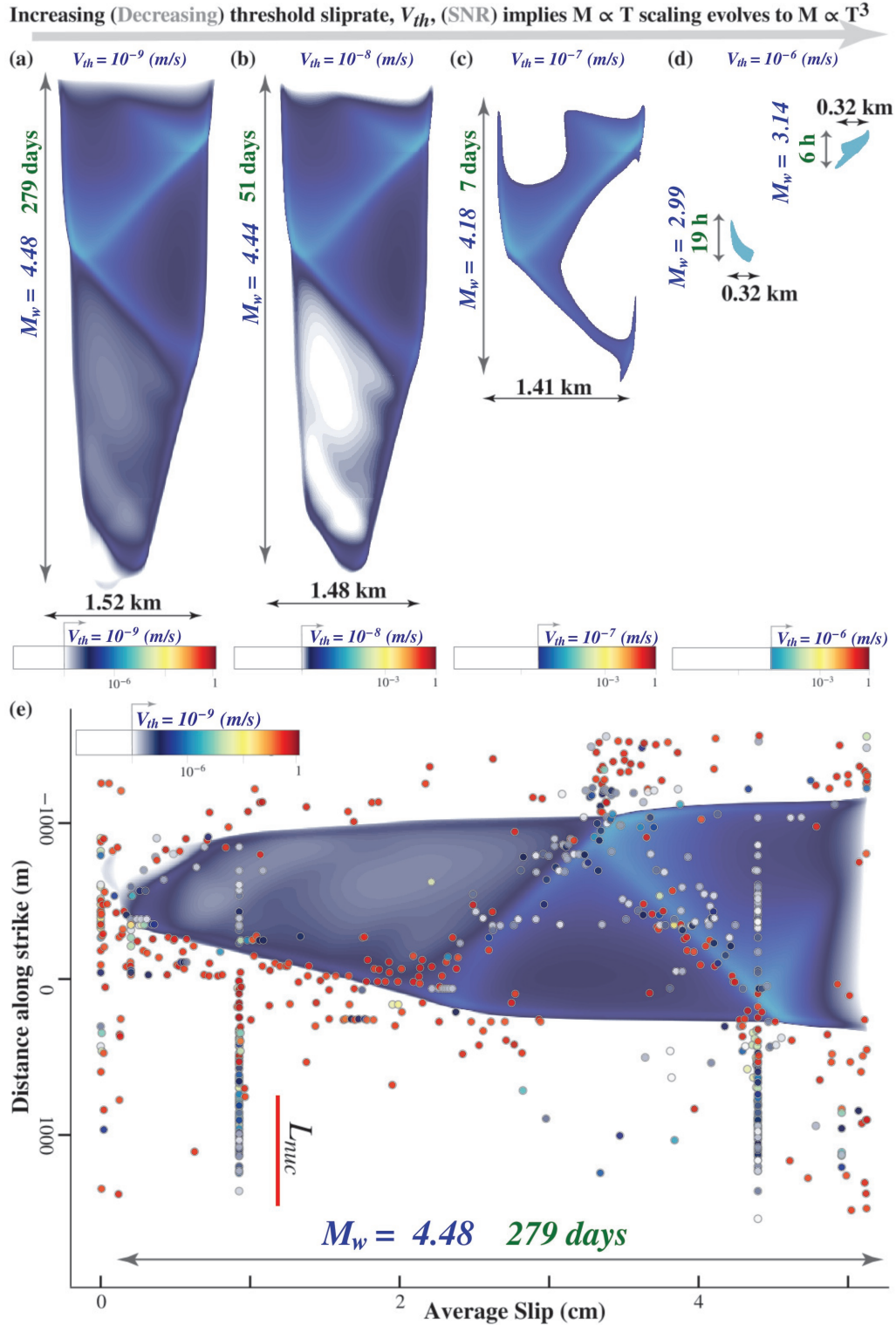


Figure 7: Effect of slip rate threshold (V_{th}), or signal to noise ratio (SNR), on the inference of the magnitude and duration of a slow slip event. The slip rate is plotted with four different minimum detection levels: (a) 10^{-9} m/s, (b) 10^{-8} m/s, (c) 10^{-7} m/s, and (d) 10^{-6} m/s. (e) Same as (a) with off-fault seismicity. Circles represent ruptures on the off-fault fractures, and are color-coded with respect to their maximum slip rate.

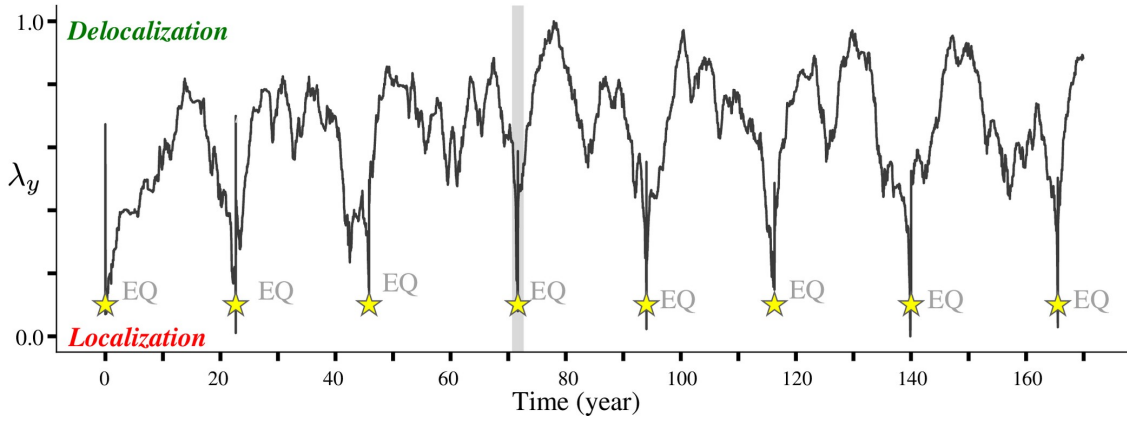


Figure 8: Localization and delocalization of off-fault seismic activity, measured by the standard deviation of hypocentral distances from the main fault in sequential 500-event batches, λ_y . The timing of earthquakes is indicated by yellow stars. The standard deviation values are normalized by their maximum value over all batches. The gray region highlights the time window shown in Figure 9.

tances from the main fault (λ_y) in sequential 500-event batches and normalize the values between 0 and 1. The events tend to localize toward the main fault plane when $\lambda_y \rightarrow 0$ and delocalize into the damage zone when $\lambda_y \rightarrow 1$. Figure 8 shows the time series of λ_y . A reduction in this time series before the main fault earthquake, followed by an increase after it, is clearly distinguishable, highlighting the localization of seismicity onto the main fault as the time of the mainshock approaches, and its delocalization after the occurrence of the earthquake.

A closer look at the location of off-fault events reveals a migration toward the epicenter of the upcoming mainshock. We observe this feature somewhat systematically in our simulations but show only the visually clearest example below. Figure 9 shows the location of off-fault events during the time interval highlighted by the gray hatch in Figure 8. Specifically, Figure 9a shows a one-year window of foreshocks, while Figure 9b shows a one-year window of aftershocks. Events are shown by circles, color-coded based on time to failure in panel (a) and time from failure in panel (b). This figure clearly illustrates the migration of off-fault events toward the epicenter, emphasizing the importance of refined event catalogs for detecting such patterns and their potential forecasting value as a mainshock approaches. Following the rupture on the main fault, λ_y increases, and off-fault seismicity no longer exhibits a migration pattern.

4.6 Apparent Diffusion

It has been observed that the migration of seismicity in some fault zones follows a specific time-space curve, similar to the one obtained from fluid diffusion (*e.g.*, Danré et al. 2024). In other words, the distance r from the epicenter versus the time from the main shock t is observed to be $r \propto D\sqrt{t}$. This may seem surprising if one attributes pore pressure dif-

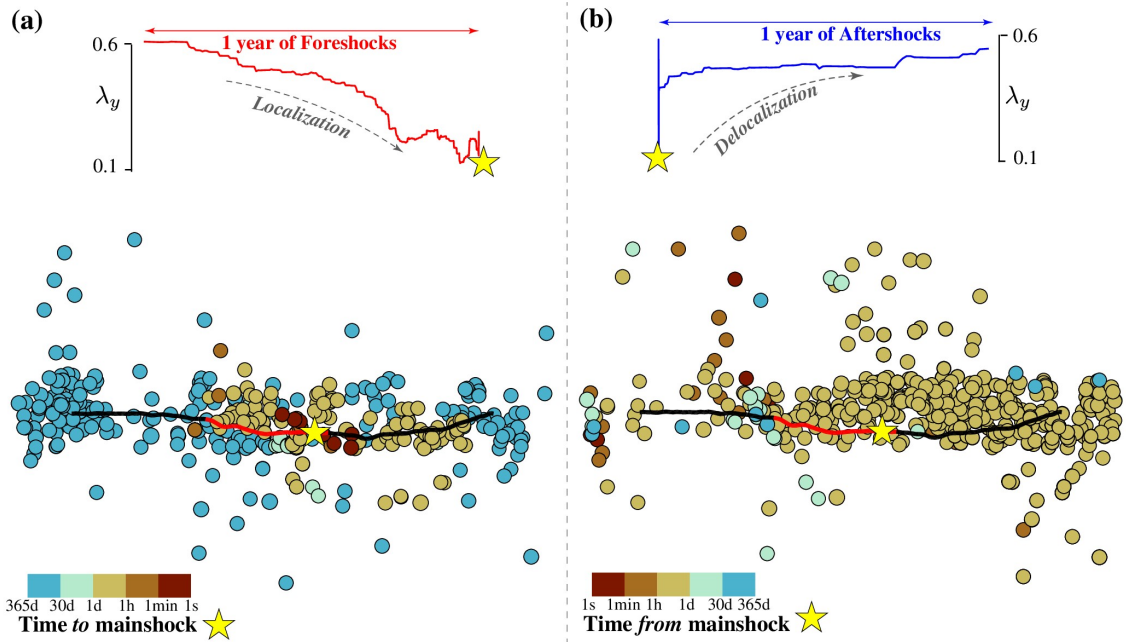


Figure 9: Zoomed-in view of the gray-hatched window shown in Figure 8, illustrating the standard deviation of the fault-normal component of earthquake locations over a one-year window before (a) and after the earthquake (b): Migration of seismicity toward the future epicenter during the foreshock period, followed by a return to background seismicity after the earthquake. Events are shown as circles, color-coded by time before and after the rupture.

fusion in a medium with uniform hydraulic properties as the only physical mechanism that gives rise to this scaling. In our simulations, we observe the same trend despite the absence of any underlying fluid diffusion process. This observation is illustrated in Figure 10, where two slow-slip ruptures are shown (panels a–c) along with seismic events occurring off-fault overlaid on the slip rate panels. The relative distance is calculated as the distance between the off-fault event and the detected nucleation point on the main fault, using a slip rate threshold of 10^{-9} m/s. The relative time is determined by the time difference between the occurrence of the off-fault event and that of the main fault. This off-fault seismicity migration is shown in panels (b–d). The values of the perceived diffusivity parameter D (0.02–0.06 m²/s) fall within the observed range for the fluid diffusivity parameter (Amezawa et al. 2021).

Our simulation thus reveals an apparent diffusive process that is driven by the slow slip process, putting a major caveat about inferring underlying fluid-driven processes just from looking at the migration of seismicity following $r \propto D\sqrt{t}$. This behavior can also emerge from the physics of interacting faults governed by rate-and-state friction along with a slow slip event occurring on the main fault.

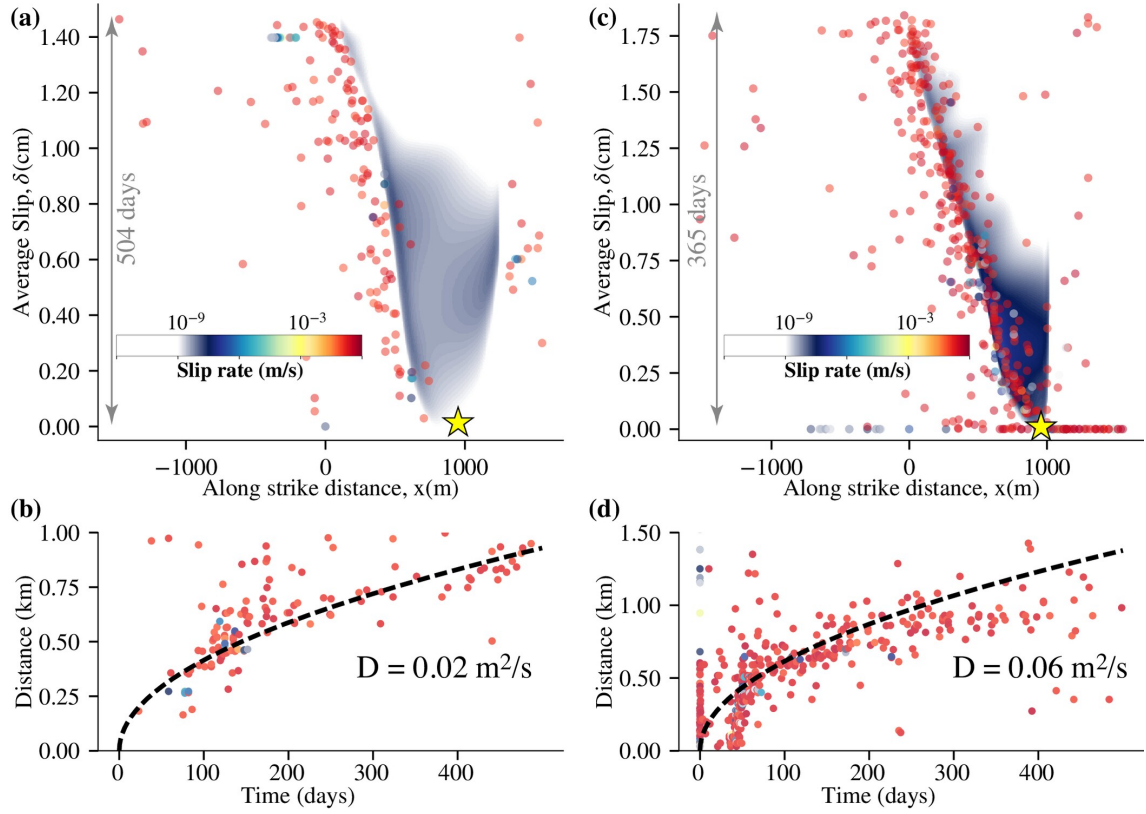


Figure 10: Off-fault Seismicity during two examples of slow-slip ruptures. a-c) Slip rate profiles of two slow slip events. b-d) The temporal migration of off-fault seismicity follows a distance from epicenter (r)–time (t) evolution (black dashed curve) similar to that of a diffusion front ($r \propto D\sqrt{t}$). The relative distance is calculated as the distance between the off-fault seismicity and the detected nucleation point on the main fault, using a slip rate threshold of 10^{-9} m/s . The corresponding diffusion coefficient (D) is noted at the top of each curve.

4.7 Source Time Functions across scales

We present a general overview of the source time functions (STFs) generated within our fault system model, focusing on their variability in moment magnitude, duration, and spectral characteristics. The analysis includes moment-rate functions (MRFs) from both slow and fast events, considering a representative fault geometry in which off-fault fractures are oriented parallel to the main fault. We selected this geometry because it exhibits a particularly broad and diverse range of temporal behaviors, capturing both small-magnitude slow events and large slow slip events occurring on both off-faults and the main fault.

Figures 11a and 11b show selected MRFs from off-fault events within narrow magnitude ranges: $-0.9 \leq M_w \leq -0.8$ and $-0.3 \leq M_w \leq -0.2$, respectively. These MRFs exhibit a continuous and broad distribution of slip durations, with significant variability in their shape, ranging from abrupt moment release to smoother and more gradual evolutions. This variability highlights the influence of structural complexity and distributed defor-

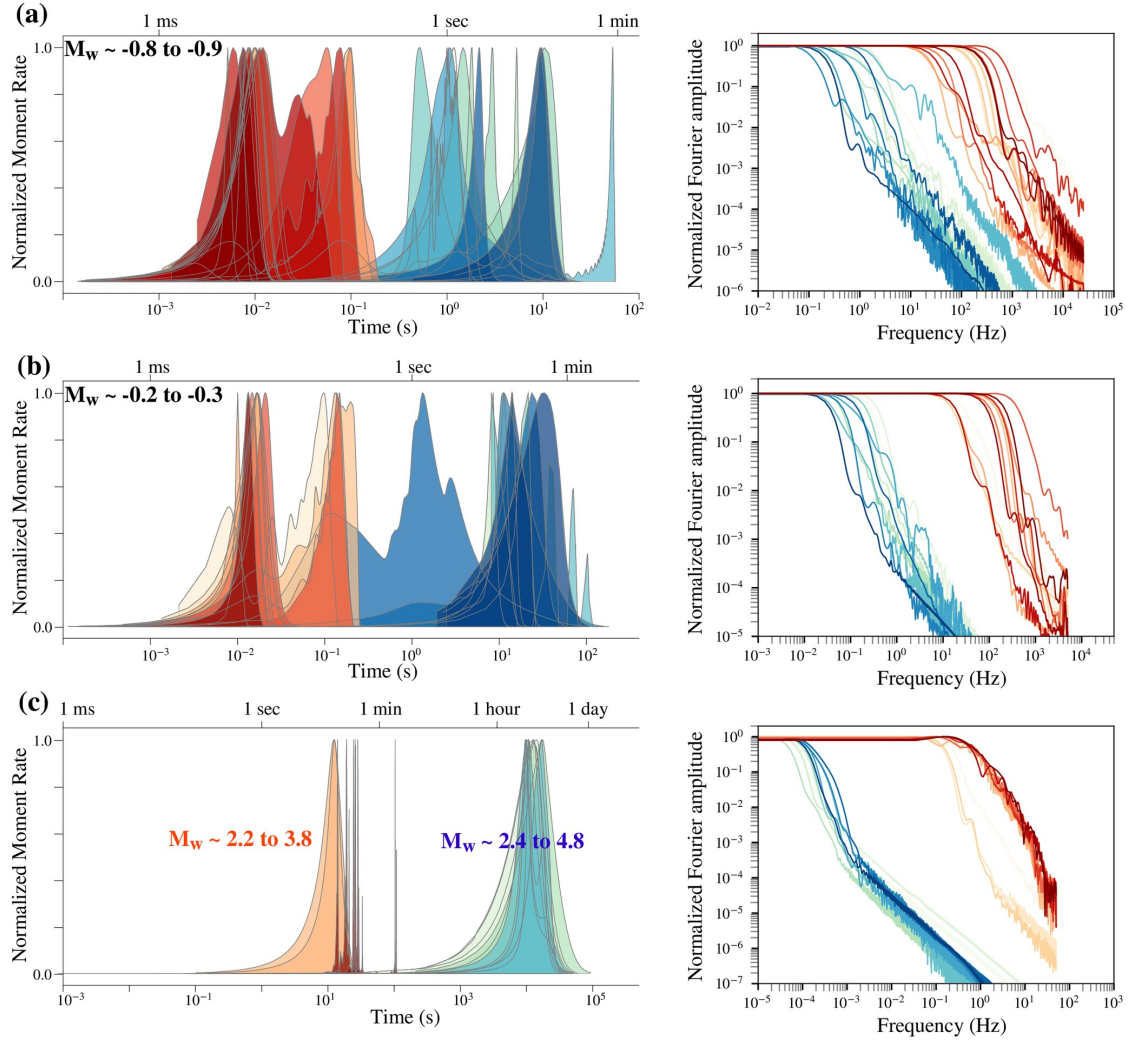


Figure 11: Moment-rate functions (MRFs) (left panels), and their spectra (right panels), across different M_w ranges for both off-fault and main fault events. (a) Selected MRFs from slow and fast events in the off-fault region within a narrow range of $-0.9 \leq M_w \leq -0.8$. (b) Same as (a), but for $-0.3 \leq M_w \leq -0.2$. (c) MRFs from main fault events, and their spectra, with a broader range of $2.2 \leq M_w \leq 3.8$ and $2.4 \leq M_w \leq 4.8$, showing both slow slip and fast rupture behavior.

mation in controlling rupture behavior, emphasizing that seismic complexity arises not only from the main fault, as shown previously, but also from off-fault activity.

Figure 11c shows MRFs of events on the main fault, which exhibit a bimodal behavior. Due to the greater extent and roughness of the main fault, the main fault hosts the largest magnitude events, characterized by more complex STFs, including multiple acceleration and deceleration phases during the ruptures. The magnitude range considered here includes both large-magnitude, fast ruptures, partial or full, ($2.2 \leq M_w \leq 3.8$) and long-duration slow slip events ($2.4 \leq M_w \leq 4.8$).

The corresponding source spectra for the same events show, as expected, that the longer durations of the slow events lead to significantly lower corner frequencies than fast

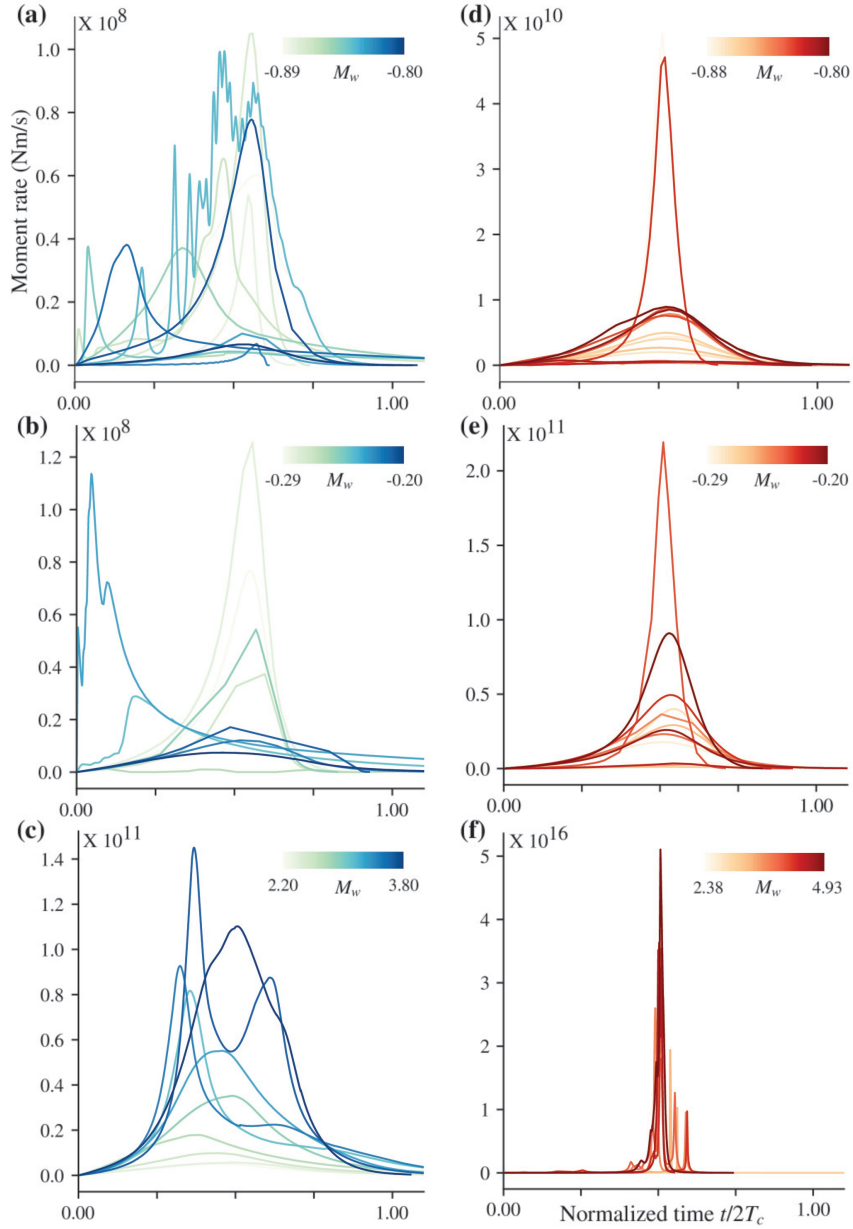


Figure 12: MRF shapes for slow and fast events after normalization by centroid time. Panels (a) and (b) correspond to slow events in the off-fault region for the same magnitude ranges as in Figures 11a and 11b. (c) shows slow events on the main fault. Panels (d) and (e) correspond to fast off-fault events with the same M_w ranges as in (a) and (b). (f) Fast events on the main fault. Color-coded by M_w .

events across all three magnitude ranges, on both the main and off-faults. Recently, [Wang et al. \(2023a\)](#) analyzed the S-wave displacement spectral signature of low-frequency earthquakes in Nankai Trough, after correcting for empirically derived attenuation, and concluded that the spectra are consistent with the classical earthquake model with vastly different rupture velocities and stress drops. Our results align very well with the conclusions drawn by [Wang et al. \(2023a\)](#). Beyond the corner frequency, the spectral decay of slow events appears similar to that of fast events. However, the high-frequency content

is less reliably estimated, as it should be predominantly influenced by the fully dynamic response of both event types, an aspect that our quasi-dynamic model does not account for but we aim to address in future investigations. To further examine MRF characteristics across these events, we normalized the time axis of each MRF with respect to its centroid time, T_c (Figure 12), defined following (Dziewonski *et al.* 1981; Duputel *et al.* 2013) as:

$$T_c = \frac{\int_{t_1}^{t_2} t \dot{M}_0(t) dt}{\int_{t_1}^{t_2} \dot{M}_0(t) dt}, \quad (1)$$

where $\dot{M}_0(t)$ is the moment rate, and t_1 and t_2 correspond to the onset and termination times of the MRF, defined by when the slip rate crosses a detection threshold.

One key distinction between slow and fast STFs lies in their symmetry. MRFs of slow events (Figures 12a–b–c) tend to be more asymmetric, typically exhibiting a sharp rise followed by a longer, gradual decay—indicating a positively skewed moment release. In contrast, fast earthquakes generally show more symmetric MRFs with a single, well-defined peak (Figures 12d–e–f). However, for the largest slow slip events (Figure 12c), the STFs of both fast and slow events become more irregular, and the asymmetry for some events is less distinguishable. Consistent with the findings of Meier *et al.* (2017), our results suggest that fast earthquakes tend to have simpler MRFs, with fewer subevents and with a well-defined peak and gradual decay (Figures 12d–e–f). While this section focuses on a specific fault geometry, similar results were obtained for an alternative fault configuration with different off-fault orientations.

5 Sensitivity Analysis of Fault Volume Model to Fracture Orientation and Friction Parameters

To assess the sensitivity of our fault volume model to various parameters, we conducted multiple simulations exploring different fracture orientations and frictional parameters of off-fault fractures. These simulations encompassed four main scenarios: right-lateral fractures (oriented at $\theta = 150^\circ \pm 10^\circ$), left-lateral fractures (oriented at $\theta = 90^\circ \pm 10^\circ$), both right and left-lateral fractures (conjugate planes at $\theta = [90^\circ; 150^\circ] \pm 10^\circ$), and fractures parallel to the major fault (oriented at $\theta = 0^\circ \pm 10^\circ$). To ensure robustness, each orientation was subjected to five different statistical samplings, guaranteeing a comprehensive understanding of the system's behavior across various geometries. Furthermore, we repeated the entire analysis, initially with an a/b ratio of 0.5 for the off-fault fractures, and subsequently with a new a/b ratio of 0.4, while maintaining homogeneous, rate-weakening friction conditions. In total, we tested 40 different configurations with various combinations of off-fault fracture orientations and frictional parameters. Our in-

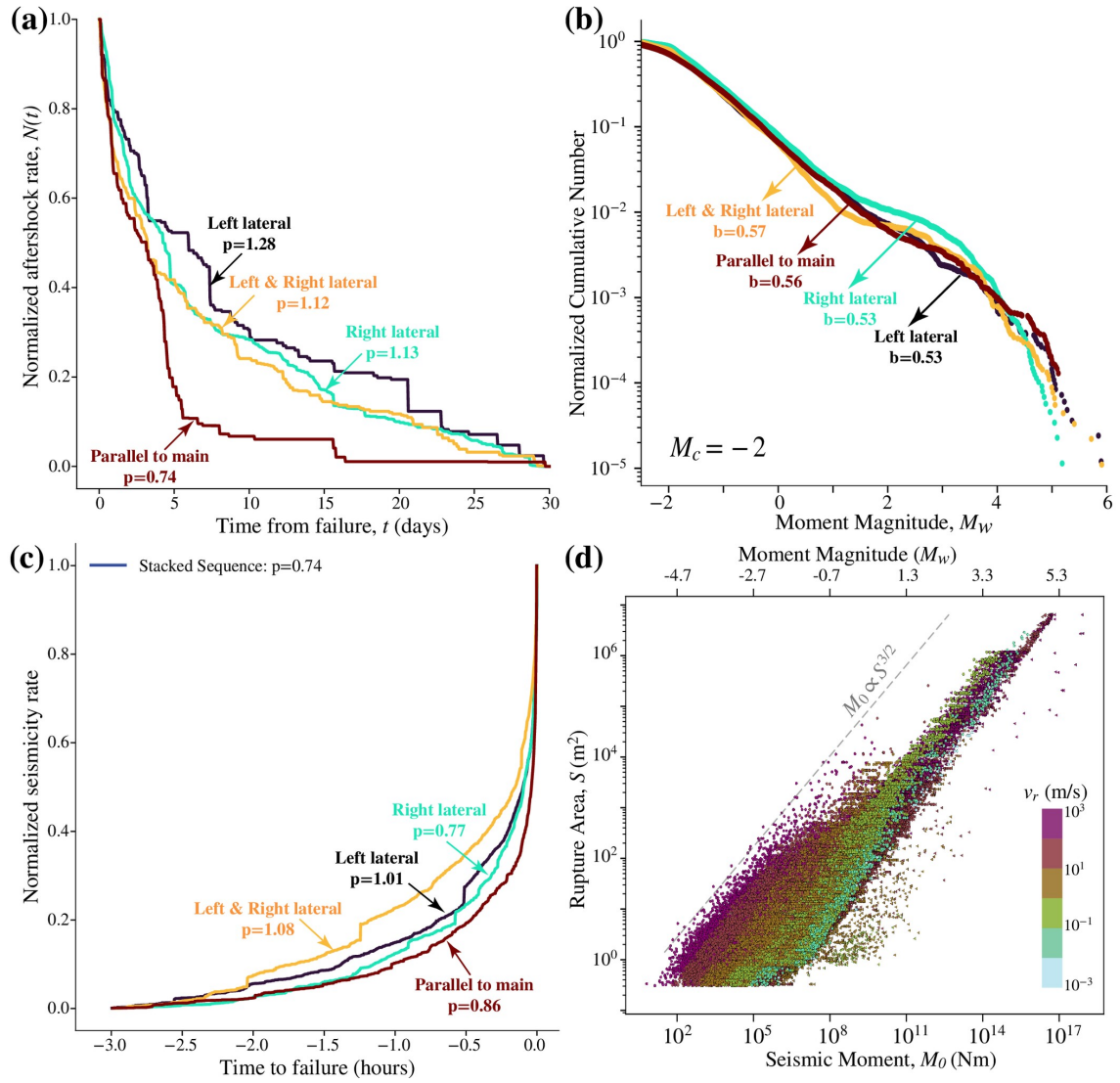


Figure 13: (a) Effect of off-fault fracture orientation on the Omori law: The average Omori decay curve over a period of 30 days is calculated from the stacked curves of different fracture orientation, and the average p coefficient is reported (b) Effect of off-fault fracture orientation on the b -value found from stacked catalog of fast ruptures with same off-fault fracture orientation (c) Effect of off-fault fracture orientation on the inverse Omori law (d) Effect of off-fault fracture orientation on the moment-area scaling. The a/b ratio of the off-fault fractures is 0.5.

investigation focuses on how these parameters influence key aspects of the statistics and scaling laws for the fault volume, and by doing so what controls the slip dynamics within the fault volume.

Figure 13a illustrates the Omori law coefficient p across different fracture orientations when $a/b = 0.5$. Remarkably, the coefficient remains consistently around 1 across all orientations, indicating a uniform behavior regardless of these parameters. While off-fault orientation does influence the duration of the aftershock period (see the case when off-faults are aligned with the main fault), we defer this investigation to future studies as it falls outside the scope of our current research. In Figure 13b, we show the Gutenberg-

Richter relationship across various fracture orientations. Remarkably, all plotted distributions conform to the Gutenberg-Richter law, displaying a similar b -value across orientations. Interestingly, there is no apparent influence of off-fault fracture orientation on the magnitude-frequency distribution, suggesting that this aspect does not significantly impact slip dynamics. Figure 13c shows the increasing rate of seismicity in a 3-hour window prior to the main shock for $a/b = 0.5$, grouped by fracture orientation. The increasing rate of seismic events off-fault exhibits an inverse Omori law, with p -values close to 1.

Figure 13d demonstrates moment-rupture area scaling (for various orientations of off-fault fractures), depicting a proportional relationship between moment and rupture area raised to the power of $3/2$ ($M_0 \propto S^{3/2}$). This scaling law underscores the fault volume model's fidelity in capturing the spatial distribution of seismic energy release across various rupture sizes. Importantly, the observation that both fast and slow ruptures exhibit almost the same scaling between moment and rupture area is noteworthy. As seismic moment is equal to stress drop multiplied by rupture area $M_0 = \Delta\sigma S^{3/2}/C$ where C is a constant and $\Delta\sigma$ is the stress drop (Kanamori & Brodsky 2001), this suggests that stress drop varies at much over fewer orders of magnitudes than rupture velocity.

Our analysis across various fracture orientations and frictional parameters reveals consistent slip dynamics. Despite orientation or a/b ratio variations, our fault volume model consistently reproduces the broad set of observations. We observe increased activity compared to single fault scenarios, with minimal influence from fracture orientation on recurrence time, event frequency, or Omori law coefficient. Additionally, the magnitude-frequency distribution remains consistent across orientations. These findings underscore the robustness of our model in capturing seismic processes and suggest its applicability to real-world scenarios. Furthermore, while fracture orientation may impact the intricacies of slip dynamics within the damage zone, such as the spatial distribution of foreshocks and aftershocks or the occurrence of cascading ruptures, these details are beyond the scope of our current study. Future investigations will delve into these aspects for a comprehensive understanding of fault behavior.

In Figure 14, we present a comprehensive catalog compiled from all simulations conducted, totaling around 1 million events, providing insight into the broad statistical features characterizing seismic activity within the fault volume model. Figure 14 illustrates moment-duration scaling, revealing a consistent relationship where moment is proportional to the cube of duration for both fast and slow ruptures. As discussed in Section 4.2, we once again notice the sensitivity of this scaling to the slip rate threshold, which may reflect the detection thresholds of seismograms and GPS stations in the field. From Figures 14a and 14b, we observe small events tend to have a continuum of rupture velocities; however, as events become larger, a distinct gap emerges between fast and slow ruptures. This gap mirrors observations reported by Ide & Beroza (2023), suggesting events that are challenging to detect or exceedingly rare. Our numerical model's ability to detect these

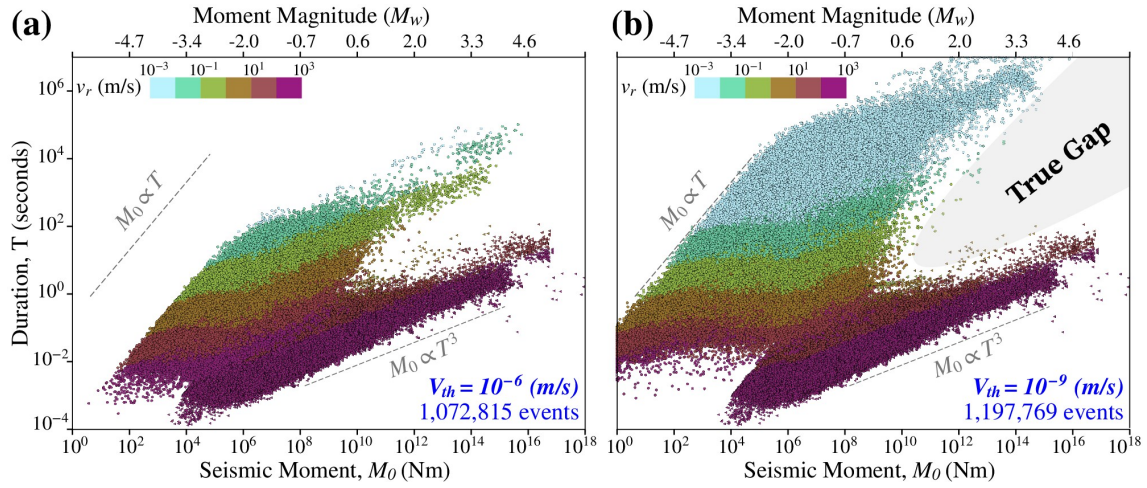


Figure 14: Moment-duration scaling for the comprehensive catalog compiled from all simulations : a) with a threshold of detection of slow ruptures at 10^{-6} m/s, showing a $M_0 \propto T^3$ relation for fast and slow ruptures; b) with a threshold of detection of slow ruptures at 10^{-9} m/s. Events are color-coded based on rupture velocity v_r .

events with confidence reinforces the presence of this gap, raising the possibility of a mechanical constraint where large events predominantly exhibit either fast or slow rupture velocities, rather than a continuum. This strongly suggests that both fast and slow ruptures may originate from the same mechanical model, despite their differing rupture velocities.

6 Discussion

These findings, when taken in total, highlight the fault volume framework's capacity to capture global, fault-related scaling laws and statistics, both on the main fault and within the fractured medium. Moreover, the fault volume model accurately reproduces diverse slip dynamics, such as large slow slip events, low-frequency earthquakes (LFEs), and earthquakes, all within a unified framework. Although it is not explored here, tectonic tremors can be explained as well with our model framework as successive rupture of shear cracks as recently proposed by *Yabe & Ujiie (2025)*. Our simulations also replicate the observed localization of deformation leading up to a rupture and subsequent delocalization of deformation into the fractured medium afterward, as recently reported by *Kato & Ben-Zion (2020)* and *Ben-Zion & Zaliapin (2020)*. This comprehensive representation of seismic activity underscores the importance of considering fault volume effects in seismic simulations. While several models produce one, or many, of the above-discussed features, the fault volume model stands out as the first to reproduce the entirety of observations and statistics simultaneously, demonstrating its efficacy in capturing the multifaceted nature of seismicity within fault systems. We note here this is not the first attempt in our community to explain the diversity of slip dynamics. In the late 1970's and early 1980's there was a flurry of papers by *Blandford (1975)*, *Nur (1978)*, *Aki*

(1979), *Andrews (1981), Hanks & McGuire (1981), and Gusev (1983)* (among many others) that have proposed heterogeneities in tractions, friction and material properties play a major role in fault mechanics. Within this historical context, our work provides a natural framework to introduce traction heterogeneities through geometric complexity and reproduces a broader spectrum of slip dynamics than just earthquakes.

This fault volume model achieves all of the above without the explicit incorporation of frictional heterogeneity or fluid presence within the medium, indicating its efficacy in explaining complex slip behaviors solely through geometric complexity, which is an independently measurable quantity. A notable distinction arises when comparing the behavior of a single fault with frictional heterogeneity to that of a fault volume. In the former case, frictional properties remain constant throughout seismic cycles, while with a fault volume model, traction (or stress) heterogeneities (asperities or barriers) naturally develop and disappear over various spatiotemporal scales. What may appear as a barrier, region of high-coupling for example, during one seismic cycle (few decades) may become an asperity during the next cycle, and vice-versa. This raises the question of what we mean by “barriers” in the context of geodetic observations, which typically span only a few decades. Such observations are often interpreted as evidence of frictional asperities, yet in reality they simply show that slip occurs when fault traction exceeds frictional resistance. Slip dynamics - whether creep, slow slip events (SSEs), or earthquakes - are additionally governed by the temporal evolution of stresses: they also control the nucleation length and thus determines whether the fault can accelerate to seismic slip velocities. Moreover, no matter how good observations become, it will be impossible to determine the frictional heterogeneity of a fault unless very strict model assumptions are made. Therefore, we argue that modeling the full spectrum of slip dynamics through geometric complexity offers a simpler, integrated, and comprehensive approach.

7 Conclusion

In this paper, we investigate how fault zone architecture can reproduce the observed spectrum of slip dynamics and their statistical properties. We perform quasi-dynamic simulations on randomly generated 2D fault zone models, where the fault zone consists of a main fault with self-similar roughness and a power-law size distribution of off-fault fractures spanning lengths from about 1 meter to kilometers. The off-fault fracture density decays with distance from the main fault, over a few cohesive zone length scales, following a power-law distribution. All faults are assigned spatially uniform, rate-weakening frictional properties ($a/b < 1$), and the critical slip distance d_c is scaled with fault length. We show that these ingredients are sufficient to reproduce the full spectrum of slip dynamics, from slow slip events to fast earthquakes, and their statistical properties.

Our simulations reproduce many natural features, including the Gutenberg-Richter magnitude-

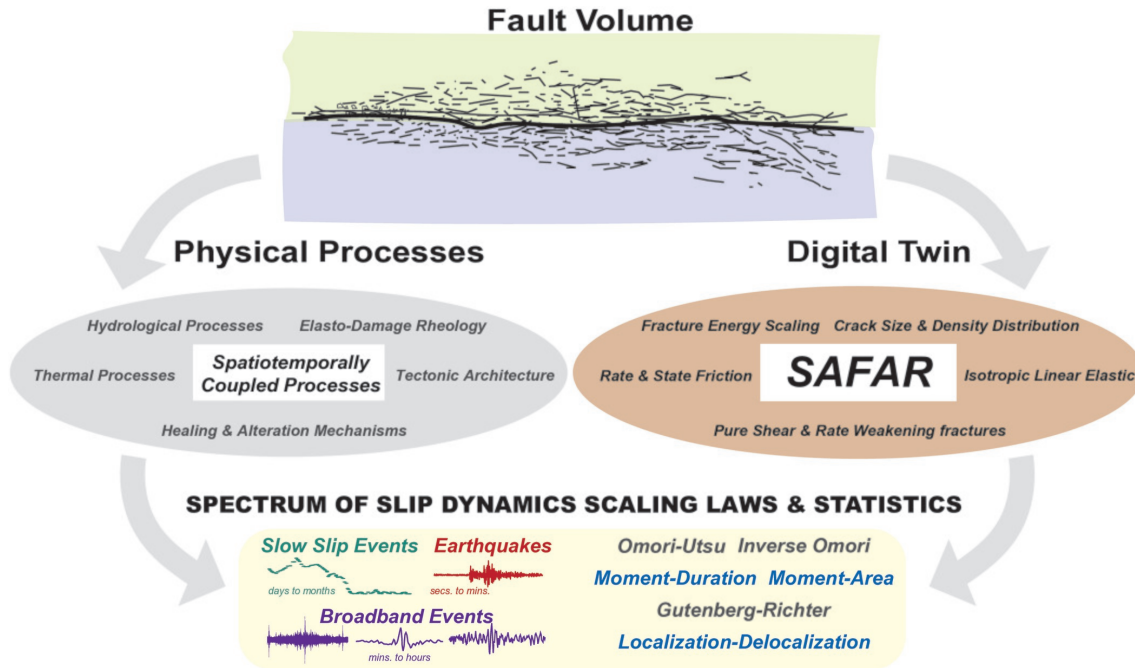


Figure 15: Summary of the digital twin model, SAFAR, that reproduces broadband slip dynamics, statistics and scaling laws of a fault volume.

frequency distribution, Omori and inverse-Omori behavior of seismicity rates before and after mainshocks, moment–duration and moment–area scaling relationships, and the observed localization-delocalization of seismicity around an event. We also observe that off-fault seismicity migrates in a manner similar to fluid diffusion in a homogeneous porous medium and raise a caveat emptor that square-root-time-like migration can emerge from the physics of interacting faults governed by rate-and-state friction, even in the absence of fluid diffusion.

Through an extensive analysis of the moment rate functions (MRFs), we find that off-fault MRF durations are continuous, whereas MRFs on the main fault show a bimodal behavior—i.e., either slow slip events or large fast earthquakes emerge. Additionally, the MRFs of small-magnitude slow-slip events tend to be asymmetric, while those of fast-slip events display a more symmetric pattern. As magnitude increases, the MRFs exhibit more pronounced acceleration and deceleration phases, deviating from simple functional forms and revealing complexities such as multiple phases of moment release.

Despite its simplicity and reliance on broadly accepted assumptions, the fault volume model presented in this paper successfully reproduces many of the observed key physical and statistical features of a canonical fault zone, making it a true digital twin of a fault zone (see Figure 15). We name this digital twin, *SAFAR* (Système Analogue des FAilles Réelles). This breakthrough opens transformative possibilities: our synthetic catalogs can enhance machine learning algorithms for seismic hazard forecasting by providing physically consistent training data that spans the full spectrum of seismic behaviors. It also

provides invaluable data to analytically model various physical mechanisms that are at the root of the observed scaling laws, statistics and slip dynamics. In addition, it can now be used to characterize the response of a fault system to various types of perturbations, such as fluid injection or earth tides, and to understand the underlying physics of earthquake triggering. Most importantly, by demonstrating that geometric complexity alone-without invoking unmeasurable frictional heterogeneities-can explain the rich fault dynamics, this work fundamentally shifts how we conceptualize and model earthquake systems, paving the way for more predictive and physically grounded seismic hazard assessment in the future.

Acknowledgements

MA, NK, CV, JC, AG and HSB gratefully acknowledge the European Research Council (ERC) for its full support of this work through the PERSISMO grant (No. 865411). MYT acknowledges support from the Agence National de la Recherche (ANR) IDEAS contract ANR-19-CE31-0004-01. PR acknowledges support from the GPX program, funded by the Agence National de la Recherche (ANR), CGG, TOTAL, and Schlumberger for his PhD fellowship and the European Research Council (ERC) Starting Grant 101040600 (HYQUAKE). NK acknowledges funding from Horizon Europe (ChEESE-2P project, grant agreement No. 101093038) for partial support in working on this manuscript. This paper has benefited from kind discussions and feedbacks from Satoshi Ide, Hideo Aochi, Romain Jolivet and Raul Madariaga. The numerical simulations presented in this study were performed on the MADARIAGA cluster, also supported by the ERC PERSISMO grant. We also used LLM models like GPT-4 and Claude to debug and optimize our codes.

Open Research Section

The datasets generated and analyzed during this study, and codes used to analyze, are available on the Zenodo repository: <https://doi.org/10.5281/zenodo.17061565>.

Appendix A Model of earthquake cycle

A1 Governing equation

A classic model of earthquake cycles contains: (1) an elastic medium that stores strain energy, (2) a physical mechanism that loads the system (plate tectonics), and finally (3) a frictional resistance on the fault, that allows the accumulation of strain on the fault. To build the model of earthquake cycles in this paper, we will use the linear momentum balance equation that states that the stress loading on the fault, and the elastic stress response due to a slip distribution on the fault, must be equal to the strength of this fault at each curvilinear point s along the fault. Mathematically, it is written as:

$$\tau^f(s) = \tau_t^{\text{el}}(s) + \tau^{\text{rad}}(s) + \tau^{\text{load}}(s) \quad (\text{A1})$$

Where $\tau^f(s)$ is the strength (model by a friction law) of the fault, $\tau_t^{\text{el}}(s)$ is the elasto-static tangential traction response due to the slip distribution on the fault, $\tau^{\text{rad}}(s)$ is the instantaneous response of the system that allows some inertia control (*Rice 1993*), these two latter modeling the reaction of the elastic medium due to the slip. Finally, $\tau^{\text{load}}(s)$ is the loading shear traction on the fault. Each of these terms will be described with more detailed in the following sections.

A2 Strength of the fault

We will model the strength of the fault by the regularized rate-and-state friction law (*Lapusta et al. 2000*):

$$\tau^f(s, t) = -f(V, \theta)\sigma_n(s, t) = -a\sigma_n(s, t) \sinh^{-1} \left[\frac{V(s, t)}{2V_0} \exp \left\{ \frac{f_0 + b \ln[V_0\theta(s, t)/d_c]}{a} \right\} \right] \quad (\text{A2})$$

with aging state evolution (*Dieterich 1979; Ruina 1983*):

$$\frac{d\theta(s, t)}{dt} = 1 - \frac{\theta(s, t)V(s, t)}{d_c} \quad (\text{A3})$$

a is the direct effect parameter that governs the instantaneous change in friction with a change in slip rate, b is the the evolution effect parameter which controls how friction evolves over time via changes in the state variable, d_c is the characteristic slip for state evolution, V_0 is reference slip rate and f_0 is the reference friction at V_0 . V and θ represent respectively the slip velocity and the state variable. σ_n is the normal traction on the fault

and d_c is the critical slip distance. The term $f_0 + b \log(V_0 \theta / d_c)$ is sometimes denoted by Ψ .

A3 Elastostatic response of the fault due to a slip distribution

The normal traction and tangential traction on the fault, given a slip distribution $\Delta \mathbf{u}(s)$, and the fault local curvature $\kappa^t(s)$, in an infinite and homogeneous medium can be calculated using boundary element method (*Tada & Yamashita 1997; Romanet et al. 2020; Romanet et al. 2024*). For convenience we will note the tangential slip on the fault $\Delta u_t(s) = \mathbf{t}(s) \cdot \Delta \mathbf{u}(s)$:

$$\tau_t^{\text{el}}(s) = \mathbf{t}(s) \cdot \bar{\sigma}(\mathbf{y}(s)) \cdot \mathbf{n}(s) = \int_{\Gamma} K_{\text{grad}}^t(s, \xi) \frac{\partial}{\partial \xi} \Delta u_t(\xi) d\xi + \int_{\Gamma} K_{\text{curv}}^t(s, \xi) \kappa^t(\xi) \Delta u_t(\xi) d\xi \quad (\text{A4})$$

$$\sigma_n^{\text{el}}(s) = \mathbf{n}(s) \cdot \bar{\sigma}(\mathbf{y}(s)) \cdot \mathbf{n}(s) = \int_{\Gamma} K_{\text{grad}}^n(s, \xi) \frac{\partial}{\partial \xi} \Delta u_t(\xi) d\xi + \int_{\Gamma} K_{\text{curv}}^n(s, \xi) \kappa^t(\xi) \Delta u_t(\xi) d\xi \quad (\text{A5})$$

In order to set the model of earthquake cycle, we chose the compression negative sign convention. s is the curvilinear location along the fault, $\Gamma \equiv \mathbf{y}(s)$, at which the stress is evaluated. ξ is a curvilinear location, at which a source of stress is located. $\mathbf{n}(\xi)$ and $\mathbf{t}(\xi)$ are respectively the normal and tangential vector to the fault at point ξ . Their component in the global coordinate system are written with the corresponding subscript. Finally, K_{grad}^t is the kernel the kernel for the tangential traction, and K_{grad}^n and K_{curv}^n are the kernel for the normal traction. K_{grad}^t and K_{curv}^t are the kernel for the tangential traction associated respectively to the effect of the gradient of tangential slip and local curvature that multiplies the tangential slip. They both derive from the fact that a derivative of the tangential slip vector along the fault is:

$$\begin{aligned} \frac{\partial}{\partial \xi} [\Delta u_t(\xi) \mathbf{t}(\xi)] &= \frac{\partial}{\partial \xi} [\Delta u_t(\xi)] \mathbf{t}(\xi) + \Delta u_t(\xi) \frac{\partial}{\partial \xi} \mathbf{t}(\xi) \\ &= \frac{\partial}{\partial \xi} [\Delta u_t(\xi)] \mathbf{t}(\xi) + \Delta u_t(\xi) \kappa^t(\xi) \mathbf{n}(\xi) \end{aligned} \quad (\text{A6})$$

where we have used the relationship $\frac{\partial}{\partial \xi} \mathbf{t}(\xi) = \kappa^t(\xi) \mathbf{n}$.

Similarly, K_{grad}^n and K_{curv}^n are the kernel for the normal traction. More details about the derivation of these equations can be found in *Romanet et al. (2024)*. It should be noted here that these kernels take into account the full elastic interaction between all faults in the system, including the main fault and all off-fault fractures.

A4 Radiation damping term

The radiation damping term was first introduced by *Rice (1993)* in the context of quasi-dynamic modeling. In fact *Andrews (1980)* showed that this is the impedance of the fault (ratio of shear stress to slip velocity) in the long wavelength limit. It was later shown that this term is exactly accounting for the instantaneous shear stress drop of the fault due to sliding (*Cochard & Madariaga 1994*):

$$\tau^{\text{rad}}(s) = -\frac{\mu}{2c_s} V(s) \quad (\text{A7})$$

We use this term together with the static kernel to account for some dynamics in the system. Without this term, the slip on the fault during one event would be unbounded (*Rice 1993*).

A5 Set of ordinary differential equations for Quasi-Dynamic earthquake cycle models

Balance of forces requires the strength of the fault to be equal to the elastic shear traction (due to slip) plus the far-field loading traction plus radiation damping term (eq. A1).

By differentiating eq. A1 with time t , it can be recast into a set of coupled ODEs. The slip acceleration becomes:

$$\frac{dV(s,t)}{dt} = \frac{\dot{\tau}^{\text{load}}(s,t) + \dot{\tau}_t^{\text{el}}(s,t) + \frac{\partial f(V,\theta)}{\partial \theta} \frac{d\theta}{dt} \sigma_n(s,t) + f(V,\theta) \dot{\sigma}_n(s,t)}{\frac{\mu}{2c_s} - \frac{\partial f(V,\theta)}{\partial V} \sigma_n(s,t)} \quad (\text{A8})$$

From this equation, it is easy to see that the denominator would go to zero and hence the acceleration would go to infinity if there was no radiation damping term (*Rice 1993*).

The elastic shear traction rate is given by:

$$\dot{\tau}_t^{\text{el}}(s,t) = \int_{\Gamma} K_{\text{grad}}^t(s,\xi) \frac{\partial}{\partial \xi} V(\xi,t) d\xi + \int_{\Gamma} K_{\text{curv}}^t(s,\xi) \kappa^t(\xi) V(\xi,t) d\xi \quad (\text{A9})$$

The change of normal traction has two sources: one due from the loading rate and another one due to the reaction to slip of the elastic medium:

$$\frac{d\sigma_n(s, t)}{dt} = \int_{faults} K_{\text{grad}}^n(s, \xi) \frac{\partial}{\partial \xi} V(\xi, t) d\xi + \int_{faults} K_{\text{curv}}^n(s, \xi) \kappa^t(\xi) V(\xi, t) d\xi + \dot{\sigma}_n^{\text{load}}(s, t) \quad (\text{A10})$$

And we recall the evolution of the state variable eq. A3. This set of ODEs is then solved at each centre of element, using the Runge-Kutta 45 adaptive time step ODE solver algorithm (Cash & Karp 1990).

A6 Numerical discretisation of the Boundary Integral Equation

In order to evaluate the previous singular integrals in the sense of Cauchy principal values, we will assume piece-wise constant slip over fixed length Δs , centred on $\mathbf{y}(s_i)$. The slip is discretised as follows (Rice 1993; Cochard & Madariaga 1994):

$$\Delta u(s) = \sum_{j=1}^N \Delta u(s_j) [\mathcal{H}(s - s_j + \Delta s/2) - \mathcal{H}(s - s_j - \Delta s/2)] \quad (\text{A11})$$

where \mathcal{H} is the Heaviside function and N is the number of elements used to discretise the fault. Because the kernels imply the evaluation of the tangential vector, it is also needed to discretised it along the fault:

$$\mathbf{t}(s) = \sum_{j=1}^N \mathbf{t}(s_j) [\mathcal{H}(s - s_j + \Delta s/2) - \mathcal{H}(s - s_j - \Delta s/2)] \quad (\text{A12})$$

Then the boundary integral equations A4 and A5 become a summation:

$$\begin{aligned} \tau(s_i) &= \sum_{j=1}^N [K_t(s_i, \xi_j) - K_t(s_i, \xi_{j+1})] \Delta u_j \\ \sigma(s_i) &= \sum_{j=1}^N [K_n(s_i, \xi_j) - K_n(s_i, \xi_{j+1})] \Delta u_j \end{aligned} \quad (\text{A13})$$

The implementation of this formulation requires to calculate for each $\tau(s_i)$ (N terms) a sum over N terms (for each j), which leads to a computational complexity of $\mathcal{O}(N^2)$. It means that the computational time will grow with the square of the problem size. This makes it difficult to handle large problems with a straightforward implementation. However, for the majority of the cases, the kernel K is smooth when the source point $\mathbf{y}(\xi_j)$ is far enough from the evaluated point $\mathbf{y}(s_i)$, or in other words: $|\mathbf{y}(s_i) - \mathbf{y}(\xi_j)| \gg 1$. Several methods can be used to accelerate the evaluation of eqns. A4 and A5. The Fast Fourier Transform was the first method used to accelerate the calculation (Andrews 1985), however it requires equispaced points on the fault. The only configuration where this

can be achieved is on a simple planar fault. Fast fourier transform has been widely used in numerical models of seismic cycles (*Lapusta et al. 2000; Lapusta & Liu 2009; Chen & Lapusta 2009; Michel et al. 2017*). The Fast Multipole Method allows for considering a complex geometry, and was used by some numerical models (*Hirahara et al. 2009; Romanet et al. 2018*), however it requires an analytical development of the kernel. In this paper, we employ Hierarchical matrices which allows for an algebraic development of the kernel and thus can be applied to a large variety of problems. This approach is particularly optimal for static problems. This will be discussed in the next section.

A7 Hierarchical Matrices

Hierarchical matrices have already been used in the context of quasi dynamic modeling of faults (*Bradley 2014; Romanet 2017; Cheng et al. 2025*). Hierarchical matrices provide data-sparse approximations of non-sparse (dense) matrices (*Hackbusch 1999; Börm et al. 2003*). Hierarchical matrices provide an approximation requiring only $\mathcal{O}(N \log N)$ units of storage (instead of $\mathcal{O}(N^2)$). The two advantages of using H-matrices are that it reduces the memory for saving the full matrix of interaction, and it is also reducing the number of operations to perform the matrix-vector products. The use of H matrices is extremely pertinent in quasidynamic models. The kernel matrix of stress interaction **A13** is not changing over time, making it a suitable matrix for compression, since the most expensive part, the construction of the data-sparse representation, is performed only once, while subsequent matrix-vector products are extremely fast. The accuracy of this method is completely controlled by the tolerance set for the compression, particularly if the required minimum accuracy approaches machine precision. The mathematical formulation of hierarchical matrices is beyond the scope of this paper but is very well explained in *Börm et al. (2003), Desiderio (2017), Romanet (2017), and Cheng et al. (2025)*.

A8 Frictional length scales

Although the general answer is unavailable in the general framework of rate and state, it is possible to infer a length scale in some limiting cases for simple straight continuum faults with homogeneous frictional parameters. The first nucleation length-scale derived for continuous fault came from the spring slider modeling. If it is assumed that the stiffness of a fault k_{fault} is inversely proportional to its length, we can derive a nucleation length scale L_{nuc} (*Rice 1992*). At the critical length L_{nuc} , the stiffness of the fault equals the critical stiffness derived from a spring slider (*Rice 1992*).

$$k_c = \sigma_n \frac{b - a}{d_c} = \frac{\mu}{L_{nuc}} = k_{fault} \quad (\text{A14})$$

Thus,

$$L_{nuc} = \frac{\mu d_c}{\sigma_n(b - a)} \quad (A15)$$

By studying the nucleation on fault with rate and state resistance, Dieterich derived another nucleation length scale L_b inversely proportional to the friction parameter b (Dieterich 1992).

$$L_b = \frac{\mu d_c}{\sigma_n b} \quad (A16)$$

More recent work shows that the nucleation actually depends on the ratio a/b (Rubin & Ampuero 2005; Ampuero & Rubin 2008; Viesca 2016). Rubin & Ampuero (2005) first derived analytical solution in the limiting case where $V\theta/D_c \gg 1$ for the aging state evolution law. They showed that this assumption would remain valid only if the ratio $a/b < 0.3781$. For high a/b however, they pointed out that the coefficient $V\theta/D_c$ was nearly constant at the interior of the nucleation patch. Using that as an assumption, with energetic consideration, they were able to derive another expression for the nucleation length scale when a/b approaches 1. We can summarize their result by:

$$\begin{cases} L_{nuc} = 2 \times 1.3774 L_b & 0 \leq a/b < 0.3781 \\ L_{nuc} = 2 \times \frac{L_b}{\pi(1 - a/b)^2} & a/b \rightarrow 1 \end{cases} \quad (A17)$$

The nucleation length scale found by Rubin & Ampuero (2005), was later shown to hold true by recasting the system of equations to look for instabilities and doing a linear perturbation analysis of these instabilities (Viesca 2016).

Appendix B Catalog building algorithm

To identify events that are spatiotemporally contiguous we use a method called Connected Component Labeling with Bounding Box Extraction. Several widely used software packages support connected component labeling (CCL) and region property extraction. In MATLAB, the `bwlabel` and `regionprops` functions provide robust tools for labeling and extracting geometric features such as bounding boxes and centroids (The MathWorks, Inc. 2024). In Python, the `scikit-image` library offers similar functionality (Walt et al. 2014). OpenCV, a popular C++ and Python computer vision library, includes highly optimized functions for fast labeling and region statistics (Bradski 2000). In this work we decided to implement this ourselves as the algorithm is trivial and it's easier to adapt the results of our code to this algorithm (see Algorithm 1).

We first take a slip rate matrix (time, space) and convert into a binary image by setting to 0 all values that are below a velocity threshold. The algorithm then performs connected component analysis on this binary image using a recursive depth-first search (DFS) strategy to identify and label contiguous regions of foreground pixels (i.e., pixels with value

Algorithm 1 Identify events

```

1: procedure CONNECTEDCOMPONENTSWITHPROPERTIES(image, rows, cols)
2:   // image : binary matrix where 1 indicates active pixel, 0 indicates background
3:   // labels : integer matrix where each nonzero entry is the region label
4:   // properties : array of structures with min/max row/column indices per re-
   gion
5:   Initialize labels[rows, cols]  $\leftarrow$  0
6:   current_label  $\leftarrow$  0
7:   Define offsets:  $dr \leftarrow [-1, -1, -1, 0, 0, 1, 1, 1]$ ,  $dc \leftarrow [-1, 0, 1, -1, 1, -1, 0, 1]$ 
8:   for col  $\leftarrow$  1 to cols do
9:     for row  $\leftarrow$  1 to rows do
10:      if image[row, col] = 1 and labels[row, col] = 0 then
11:        current_label  $\leftarrow$  current_label + 1
12:        properties[current_label]: min/max row/col  $\leftarrow$  row, col
13:        LABELREGIONS(row, col, current_label)
14:      end if
15:    end for
16:  end for
17:  return labels, properties, current_label
18: end procedure
19: procedure LABELREGIONS(r, c, label)
20:   if r or c out of bounds or not 1 or already labeled then return
21:   end if
22:   labels[r, c]  $\leftarrow$  label
23:   Update properties[label] with min/max of r, c
24:   for i  $\leftarrow$  1 to 8 do
25:     nr  $\leftarrow$  r + dr[i], nc  $\leftarrow$  c + dc[i]
26:     LABELREGIONS(nr, nc, label)
27:   end for
28: end procedure

```

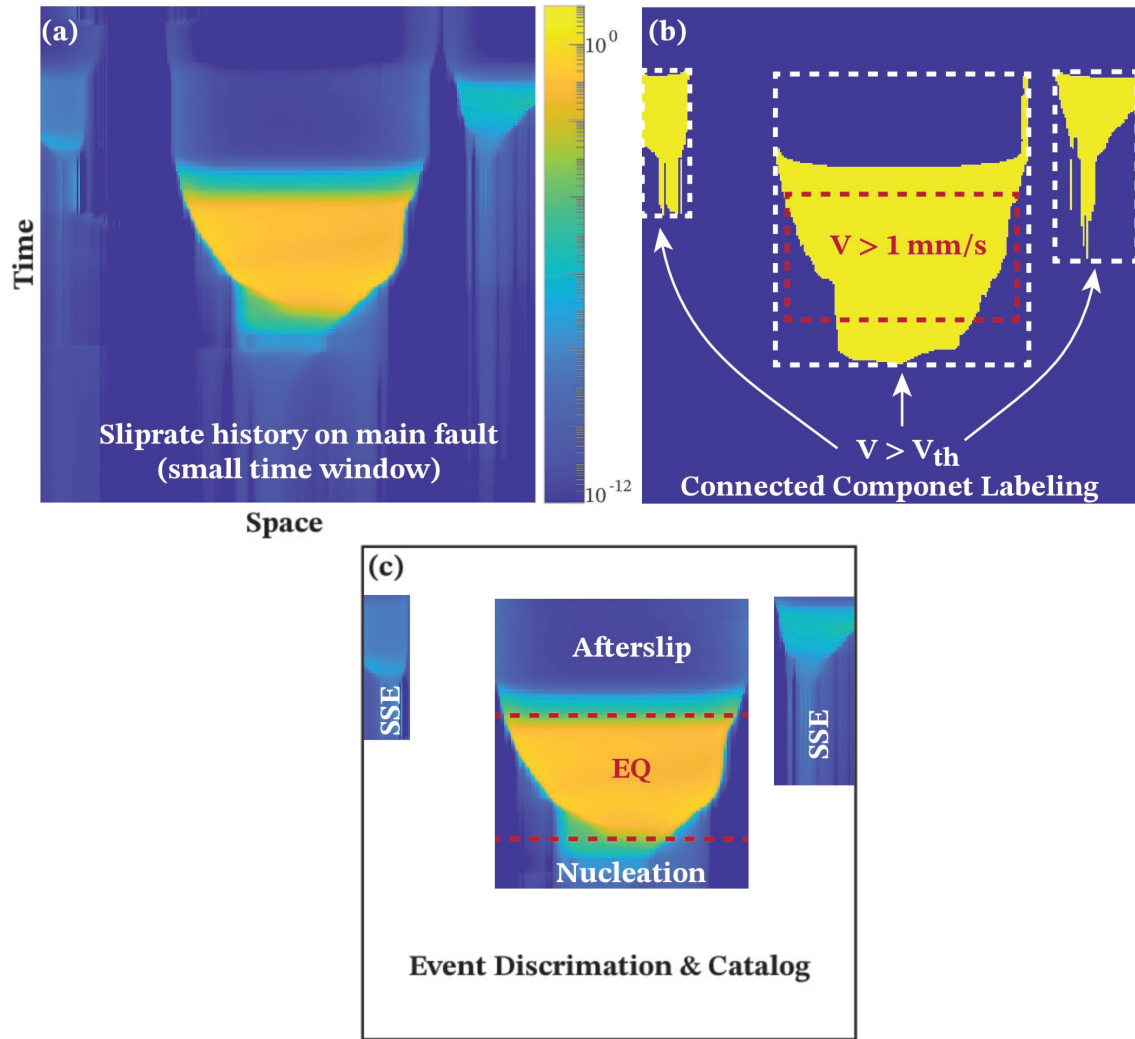


Figure B1: Steps involved in catalog generation from slip rate matrix. (a) Slip rate matrix (time, space). (b) Binary image after thresholding slip rates with Labeled connected components. (c) Bounding boxes around each connected component, representing individual events.

1). Each connected region is assigned a unique integer label, and its spatial extent is recorded as a bounding box defined by the minimum and maximum row and column indices. This type of region labeling is a fundamental technique in image analysis, commonly used for shape recognition, segmentation, and morphological operations. The DFS uses an 8-connectivity scheme, meaning that each pixel is connected to its horizontal, vertical, and diagonal neighbors. This is particularly useful in natural or irregular structures where connectivity extends beyond 4-neighbor (Manhattan) adjacency. The use of recursive DFS provides an intuitive implementation but is best suited for small to moderately sized images due to potential stack overflow risks. For larger datasets, stack-based or union-find methods may be preferred (*Rosenfeld & Pfaltz 1966; Shapiro & Stockman 2001*).

The procedure begins by scanning the image in a raster order. When an unlabeled foreground pixel is encountered, a new label is assigned, and a recursive DFS is initiated from that pixel to visit all 8-connected neighboring pixels belonging to the same region. During traversal, the algorithm updates a property array that maintains the axis-aligned bounding box for each region in the form (min_row, max_row, min_col, max_col). Once the beginning and the end of the event (min_row, max_row) and its spatial extent (min_col, max_col) are obtained it's trivial to compute the Moment, average slip, duration and other catalog based quantities.

References

- Abdelmeguid, M. & A. Elbanna (2022). "Sequences of seismic and aseismic slip on bimaterial faults show dominant rupture asymmetry and potential for elevated seismic hazard". *Earth and Planetary Science Letters* 593, p. 117648. DOI: [10.1016/j.epsl.2022.117648](https://doi.org/10.1016/j.epsl.2022.117648).
- Abercrombie, R. E. & J. R. Rice (2005). "Can observations of earthquake scaling constrain slip weakening?" *Geophysical Journal International* 162.2, pp. 406–424. DOI: [10.1111/j.1365-246x.2005.02579.x](https://doi.org/10.1111/j.1365-246x.2005.02579.x).
- Aki, K. (1965). "Maximum likelihood estimate of b in the formula $\log N=a-bM$ and its confidence limits". *Bull. Earthquake Res. Inst., Tokyo Univ.* 43, pp. 237–239.
- Aki, K. (1981). "A probabilistic synthesis of precursory phenomena". *Earthquake Prediction: An International Review, Maurice Ewing Series*. Ed. by D. W. Simpson & P. G. Richards. Vol. 4. AGU. DOI: [10.1029/ME004p0566](https://doi.org/10.1029/ME004p0566).
- Aki, K. (1979). "Characterization of barriers on an earthquake fault". *J. Geophys. Res.* 84.B11, pp. 6140–6148. DOI: [10.1029/JB084iB11p06140](https://doi.org/10.1029/JB084iB11p06140).
- Amezawa, Y., T. Maeda & M. Kosuga (2021). "Migration diffusivity as a controlling factor in the duration of earthquake swarms". *Earth, Planets and Space* 73.1. DOI: [10.1186/s40623-021-01480-7](https://doi.org/10.1186/s40623-021-01480-7).
- Ampuero, J.-P. & A. M. Rubin (2008). "Earthquake nucleation on rate and state faults—Aging and slip laws". *Journal of Geophysical Research* 113.B1. DOI: [10.1029/2007JB005082](https://doi.org/10.1029/2007JB005082).
- Ando, R., N. Takeda & T. Yamashita (2012). "Propagation dynamics of seismic and aseismic slip governed by fault heterogeneity and Newtonian rheology". *Journal of Geophysical Research* 117, B11308. DOI: [10.1029/2012jb009532](https://doi.org/10.1029/2012jb009532).
- Andrews, D. J. (1980). "Fault impedance and earthquake energy in the Fourier transform domain". *Bulletin of the Seismological Society of America* 70.5, pp. 1683–1698. DOI: [10.1785/BSSA0700051683](https://doi.org/10.1785/BSSA0700051683).
- Andrews, D. J. (1981). "A stochastic fault model: 2. Time-dependent case". *J. Geophys. Res.* 86.B11, pp. 10821–10834. DOI: [10.1029/JB086iB11p10821](https://doi.org/10.1029/JB086iB11p10821).
- Andrews, D. J. (1985). "Dynamic plane-strain shear rupture with a slip-weakening friction law calculated by a boundary integral method". *Bulletin of the Seismological Society of America* 75.1, pp. 1–21. DOI: [10.1785/bssa0750010001](https://doi.org/10.1785/bssa0750010001).
- Andrews, D. J. (2005). "Rupture dynamics with energy loss outside the slip zone". *Journal of Geophysical Research: Solid Earth* 110.B1. DOI: [10.1029/2004jb003191](https://doi.org/10.1029/2004jb003191).
- Aochi, H., E. Fukuyama & M. Matsu'ura (2000). "Selectivity of spontaneous rupture propagation on a branched fault". *Geophysical Research Letters* 27.22, pp. 3635–3638. DOI: [10.1029/2000gl011560](https://doi.org/10.1029/2000gl011560).
- Aochi, H. & S. Ide (2009). "Complexity in earthquake sequences controlled by multiscale heterogeneity in fault fracture energy". *Journal of Geophysical Research: Solid Earth* 114.B3. DOI: [10.1029/2008jb006034](https://doi.org/10.1029/2008jb006034).
- Ariyoshi, K., T. Matsuzawa, J.-P. Ampuero, R. Nakata, T. Hori, Y. Kaneda, R. Hino & A. Hasegawa (2012). "Migration process of very low-frequency events based on a chain-reaction model and its application to the detection of preseismic slip for megathrust earthquakes". *Earth, Planets and Space* 64.8, pp. 693–702. DOI: [10.5047/eps.2010.09.003](https://doi.org/10.5047/eps.2010.09.003).
- Barbot, S. (2019). "Slow-slip, slow earthquakes, period-two cycles, full and partial ruptures, and deterministic chaos in a single asperity fault". *Tectonophysics* 768, p. 228171. DOI: [10.1016/j.tecto.2019.228171](https://doi.org/10.1016/j.tecto.2019.228171).
- Ben-Zion, Y. & C. G. Sammis (2003). "Characterization of Fault Zones". *Pure and Applied Geophysics* 160.3, pp. 677–715. DOI: [10.1007/p100012554](https://doi.org/10.1007/p100012554).
- Ben-Zion, Y. & I. Zaliapin (2019). "Spatial variations of rock damage production by earthquakes in southern California". *Earth and Planetary Science Letters* 512, pp. 184–193. DOI: [10.1016/j.epsl.2019.02.006](https://doi.org/10.1016/j.epsl.2019.02.006).
- Ben-Zion, Y. & I. Zaliapin (2020). "Localization and coalescence of seismicity before large earthquakes". *Geophysical Journal International* 223.1, pp. 561–583. DOI: [10.1093/gji/ggaa315](https://doi.org/10.1093/gji/ggaa315).
- Beroza, G. C. & S. Ide (2011). "Slow Earthquakes and Nonvolcanic Tremor". *Annual Review of Earth and Planetary Sciences* 39.1, pp. 271–296. DOI: [10.1146/annurev-earth-040809-152531](https://doi.org/10.1146/annurev-earth-040809-152531).
- Bhat, H. S. (2004). "Dynamic Slip Transfer from the Denali to Totschunda Faults, Alaska: Testing Theory for Fault Branching". *Bulletin of the Seismological Society of America* 94.6B, S202–S213. DOI: [10.1785/0120040601](https://doi.org/10.1785/0120040601).
- Bhat, H. S., R. L. Biegel, A. J. Rosakis & C. G. Sammis (2010). "The Effect of Asymmetric Damage on Dynamic Shear Rupture Propagation II: With Mismatch in Bulk Elasticity". *Tectonophysics* 493.3, pp. 263–271. DOI: [10.1016/j.tecto.2010.03.016](https://doi.org/10.1016/j.tecto.2010.03.016).
- Bhat, H. S., R. Dmowska, G. C. P. King, Y. Klinger & J. R. Rice (2007a). "Off-fault damage patterns due to supershear ruptures with application to the 2001 Mw 8.1 Kokoxili (Kunlun) Tibet earthquake". *Journal of Geophysical Research: Solid Earth* 112.B6. DOI: [10.1029/2006jb004425](https://doi.org/10.1029/2006jb004425).
- Bhat, H. S., M. Olives, R. Dmowska & J. R. Rice (2007b). "Role of fault branches in earthquake rupture dynamics". *Journal of Geophysical Research: Solid Earth* 112.B11. DOI: [10.1029/2007jb005027](https://doi.org/10.1029/2007jb005027).
- Biasi, G. P. & S. G. Wesnousky (2016). "Steps and Gaps in Ground Ruptures: Empirical Bounds on Rupture Propagation". *Bulletin of the Seismological Society of America* 106.3, pp. 1110–1124. DOI: [10.1785/0120150175](https://doi.org/10.1785/0120150175).
- Biegel, R. L. & C. G. Sammis (2004). "Relating fault mechanics to fault zone structure". *Advances in Geophysics*, Vol. 44 47, pp. 65–111. DOI: [10.1016/s0065-2687\(04\)47002-2](https://doi.org/10.1016/s0065-2687(04)47002-2).

- Blandford, R. R. (1975). "A source theory for complex earthquakes". *Bulletin of the Seismological Society of America* 65.5, pp. 1385–1405. DOI: [10.1785/BSSA0650051385](https://doi.org/10.1785/BSSA0650051385).
- Bonnet, E., O. Bour, N. E. Odling, P. Davy, I. Main, P. Cowie & B. Berkowitz (2001). "Scaling of fracture systems in geological media". *Reviews of Geophysics* 39.3, pp. 347–383. DOI: [10.1029/1999rg000074](https://doi.org/10.1029/1999rg000074).
- Börm, S., L. Grasedyck & W. Hackbusch (2003). "Introduction to hierarchical matrices with applications". *Engineering Analysis with Boundary Elements* 27.5, pp. 405–422. DOI: [10.1016/s0955-7997\(02\)00152-2](https://doi.org/10.1016/s0955-7997(02)00152-2).
- Brace, W. F. & J. D. Byerlee (1966). "Stick-slip as a mechanism for earthquakes". *Science* 153.3739, pp. 990–992. DOI: [10.1126/science.153.3739.990](https://doi.org/10.1126/science.153.3739.990).
- Bradley, A. M. (2014). "Software for efficient static dislocation–Traction calculations in fault simulators". *Seismol. Res. Lett.* 85.6, pp. 1358–1365. DOI: [10.1785/0220140092](https://doi.org/10.1785/0220140092).
- Bradski, G. (2000). "The OpenCV Library". *Dr. Dobb's Journal of Software Tools*. Available at: <https://opencv.org>.
- Caballero, E., A. Chounet, Z. Duputel, J. Jara, C. Twardzik & R. Jolivet (2021). "Seismic and Aseismic Fault Slip During the Initiation Phase of the 2017 MW = 6.9 Valparaíso Earthquake". *Geophysical Research Letters* 48.6. DOI: [10.1029/2020GL091916](https://doi.org/10.1029/2020GL091916).
- Candela, T., F. Renard, M. Bouchon, A. Brouste, D. Marsan, J. Schmittbuhl & C. Voisin (2009). "Characterization of Fault Roughness at Various Scales: Implications of Three-Dimensional High Resolution Topography Measurements". *Pure and Applied Geophysics* 166.10–11, pp. 1817–1851. DOI: [10.1007/s00024-009-0521-2](https://doi.org/10.1007/s00024-009-0521-2).
- Candela, T., F. Renard, Y. Klinger, K. Mair, J. Schmittbuhl & E. E. Brodsky (2012). "Roughness of fault surfaces over nine decades of length scales". *Journal of Geophysical Research: Solid Earth* 117.B8. DOI: [10.1029/2011jb009041](https://doi.org/10.1029/2011jb009041).
- Candela, T., F. Renard, J. Schmittbuhl, M. Bouchon & E. E. Brodsky (2011). "Fault slip distribution and fault roughness: Fault slip distribution and fault roughness". *Geophysical Journal International* 187.2, pp. 959–968. DOI: [10.1111/j.1365-246x.2011.05189.x](https://doi.org/10.1111/j.1365-246x.2011.05189.x).
- Cash, J. R. & A. H. Karp (1990). "A variable order Runge-Kutta method for initial value problems with rapidly varying right-hand sides". *ACM Transactions on Mathematical Software* 16.3, pp. 201–222. DOI: [10.1145/79505.79507](https://doi.org/10.1145/79505.79507).
- Cattania, C. & P. Segall (2021). "Precursory Slow Slip and Foreshocks on Rough Faults". *Journal of Geophysical Research: Solid Earth* 126.4. DOI: [10.1029/2020jb020430](https://doi.org/10.1029/2020jb020430).
- Chalumeau, C., H. Agurto-Detzel, A. Rietbrock, M. Frietsch, O. Oncken, M. Segovia & A. Galve (2024). "Seismological evidence for a multifault network at the subduction interface". *Nature* 628.8008, pp. 558–562. DOI: [10.1038/s41586-024-07245-y](https://doi.org/10.1038/s41586-024-07245-y).
- Chen, K., G. Wei, C. Milliner, L. Dal Zilio, C. Liang & J.-P. Avouac (2024). "Super-shear ruptures steered by pre-stress heterogeneities during the 2023 Kahramanmaraş earthquake doublet". *Nature Communications* 15.1, p. 7004. DOI: [10.1038/s41467-024-51446-y](https://doi.org/10.1038/s41467-024-51446-y).
- Chen, T. & N. Lapusta (2009). "Scaling of small repeating earthquakes explained by interaction of seismic and aseismic slip in a rate and state fault model". *Journal of Geophysical Research: Solid Earth* 114.B1. DOI: [10.1029/2008jb005749](https://doi.org/10.1029/2008jb005749).
- Cheng, J., H. S. Bhat, M. Almakari, B. Lecampion & C. Peruzzo (2025). "FASTDASH: An Implementation of 3D Earthquake Cycle Simulation on Complex Fault Systems Using the Boundary Element Method Accelerated by H-matrices". *Geophysical Journal International*, ggaf230. DOI: [10.1093/gji/ggaf230](https://doi.org/10.1093/gji/ggaf230).
- Chester, F. M., J. P. Evans & R. L. Biegel (1993). "Internal structure and weakening mechanisms of the San Andreas fault". *Journal of Geophysical Research* 98, pp. 771–786. DOI: [10.1029/92jb01866](https://doi.org/10.1029/92jb01866).
- Chester, F. M. & J. M. Logan (1986). "Implications for mechanical properties of brittle faults from observations of the Punchbowl fault zone, California". *pure and applied geophysics* 124.1–2, pp. 79–106. DOI: [10.1007/bf00875720](https://doi.org/10.1007/bf00875720).
- Cochard, A. & R. Madariaga (1994). "Dynamic Faulting Under Rate-Dependent Friction". *Pure and Applied Geophysics* 142 (3–4), pp. 419–445. DOI: [10.1007/BF00876049](https://doi.org/10.1007/BF00876049).
- Colletini, C., C. Viti, S. A. Smith & R. E. Holdsworth (2009). "Development of interconnected talc networks and weakening of continental low-angle normal faults". *Geology* 37.6, pp. 567–570. DOI: [10.1130/G25645A.1](https://doi.org/10.1130/G25645A.1).
- Costantino, G., M. Radiguet, Z. El Yousfi & A. Socquet (2025). "A continuum of slow slip events in the Cascadia subduction zone illuminated by high-resolution deep-learning denoising". *Authorea*. DOI: [10.22541/au.175079869.97623047/v1](https://doi.org/10.22541/au.175079869.97623047/v1).
- Cruz-Atienza, V. M., J. Tago, C. Villafuerte, M. Wei, R. Garza-Girón, L. A. Dominguez, V. Kostoglodov, T. Nishimura, S. I. Franco, J. Real, M. A. Santoyo, Y. Ito & E. Kazachkina (2021). "Short-term interaction between silent and devastating earthquakes in Mexico". *Nature Communications* 12.1. DOI: [10.1038/s41467-021-22326-6](https://doi.org/10.1038/s41467-021-22326-6).
- Cruz-Atienza, V. M., C. Villafuerte & H. S. Bhat (2018). "Rapid tremor migration and pore-pressure waves in subduction zones". *Nature Communications* 9.1. DOI: [10.1038/s41467-018-05150-3](https://doi.org/10.1038/s41467-018-05150-3).
- Dal Zilio, L., N. Lapusta & J. Avouac (2020). "Unraveling Scaling Properties of Slow-Slip Events". *Geophysical Research Letters* 47.10. DOI: [10.1029/2020gl087477](https://doi.org/10.1029/2020gl087477).
- Danré, P., L. De Barros, F. Cappa & L. Passarelli (2024). "Parallel dynamics of slow slips and fluid-induced seismic swarms". *Nature Communications* 15.1. DOI: [10.1038/s41467-024-53285-3](https://doi.org/10.1038/s41467-024-53285-3).
- Desiderio, L. (2017). "H-matrix based Solver for 3D Elastodynamics Boundary Integral Equations". Theses. Université Paris Saclay (COMUE).

- Dieterich, J. H. (1979). "Modeling of rock friction: 1. Experimental results and constitutive equations". *Journal of Geophysical Research: Solid Earth* 84.B5, pp. 2161–2168. DOI: [10.1029/jb084ib05p02161](https://doi.org/10.1029/jb084ib05p02161).
- Dieterich, J. H. (1992). "Earthquake nucleation on faults with rate-and state-dependent strength". *Tectonophysics* 211.1-4, pp. 115–134. DOI: [10.1016/0040-1951\(92\)90055-b](https://doi.org/10.1016/0040-1951(92)90055-b).
- Dor, O., Y. Ben-Zion, T. K. Rockwell & J. N. Brune (2006a). "Pulverized rocks in the Mojave section of the San Andreas Fault Zone". *Earth and Planetary Science Letters* 245.3-4, pp. 642–654. DOI: [10.1016/j.epsl.2006.03.034](https://doi.org/10.1016/j.epsl.2006.03.034).
- Dor, O., T. K. Rockwell & Y. Ben-Zion (2006b). "Geological observations of damage asymmetry in the structure of the San Jacinto, San Andreas and Punchbowl Faults in Southern California: A possible indicator for preferred rupture propagation direction". *Pure and Applied Geophysics* 163.2, pp. 301–349. DOI: [10.1007/s00024-005-0023-9](https://doi.org/10.1007/s00024-005-0023-9).
- Douglas, A., J. Beavan, L. Wallace & J. Townend (2005). "Slow slip on the northern Hikurangi subduction interface, New Zealand". *Geophysical Research Letters* 32.16. DOI: [10.1029/2005g1023607](https://doi.org/10.1029/2005g1023607).
- Dragert, H., K. Wang & T. S. James (2001). "A Silent Slip Event on the Deeper Cascadia Subduction Interface". *Science* 292.5521, pp. 1525–1528. DOI: [10.1126/science.1060152](https://doi.org/10.1126/science.1060152).
- Dublanchet, P. (2017). "The dynamics of earthquake precursors controlled by effective friction". *Geophysical Journal International* 212.2, pp. 853–871. DOI: [10.1093/gji/ggx438](https://doi.org/10.1093/gji/ggx438). eprint: <https://academic.oup.com/gji/article-pdf/212/2/853/22068943/ggx438.pdf>.
- Dublanchet, P., P. Bernard & P. Favreau (2013). "Interactions and triggering in a 3-D rate-and-state asperity model". *Journal of Geophysical Research: Solid Earth* 118.5, pp. 2225–2245. DOI: [10.1002/jgrb.50187](https://doi.org/10.1002/jgrb.50187).
- Dunham, E. M., D. Belanger, L. Cong & J. E. Kozdon (2011). "Earthquake Ruptures with Strongly Rate-Weakening Friction and Off-Fault Plasticity, Part 2: Nonplanar Faults". *Bulletin of the Seismological Society of America* 101.5, pp. 2308–2322. DOI: [10.1785/0120100076](https://doi.org/10.1785/0120100076).
- Duputel, Z., V. C. Tsai, L. Rivera & H. Kanamori (2013). "Using centroid time-delays to characterize source durations and identify earthquakes with unique characteristics". *Earth and Planetary Science Letters* 374, pp. 92–100. DOI: [10.1016/j.epsl.2013.05.024](https://doi.org/10.1016/j.epsl.2013.05.024).
- Dziewonski, A. M., T. Chou & J. H. Woodhouse (1981). "Determination of earthquake source parameters from waveform data for studies of global and regional seismicity". *Journal of Geophysical Research: Solid Earth* 86.B4, pp. 2825–2852. DOI: [10.1029/jb086ib04p02825](https://doi.org/10.1029/jb086ib04p02825).
- Fagereng, Å., F. Remitti & R. H. Sibson (2010). "Shear veins observed within anisotropic fabric at high angles to the maximum compressive stress". *Nature Geoscience* 3.7, pp. 482–485. DOI: [10.1038/ngeo898](https://doi.org/10.1038/ngeo898).
- Faulkner, D. R., T. M. Mitchell, D. Healy & M. J. Heap (2006). "Slip on "weak" faults by the rotation of regional stress in the fracture damage zone". *Nature* 444.7121, pp. 922–925. DOI: [10.1038/nature05353](https://doi.org/10.1038/nature05353).
- Faulkner, D. R., T. M. Mitchell, E. Jensen & J. Cembrano (2011). "Scaling of fault damage zones with displacement and the implications for fault growth processes". *Journal of Geophysical Research* 116.B05403. DOI: [10.1029/2010JB007788](https://doi.org/10.1029/2010JB007788).
- Fletcher, J. M., O. J. Teran, T. K. Rockwell, M. E. Oskin, K. W. Hudnut, K. J. Mueller, R. M. Spelz, S. O. Akciz, E. Masana, G. Faneros, E. J. Fielding, S. Leprince, A. E. Morelan, J. Stock, D. K. Lynch, A. J. Elliott, P. Gold, J. Liu-Zeng, A. González-Ortega, A. Hinojosa-Corona & J. González-García (2014). "Assembly of a large earthquake from a complex fault system: Surface rupture kinematics of the 4 April 2010 El Mayor-Cucapah (Mexico) Mw 7.2 earthquake". *Geosphere* 10.4, pp. 797–827. DOI: [10.1130/ges00933.1](https://doi.org/10.1130/ges00933.1).
- Fliss, S., H. S. Bhat, R. Dmowska & J. R. Rice (2005). "Fault branching and rupture directivity". *Journal of Geophysical Research: Solid Earth* 110.B6. DOI: [10.1029/2004jb003368](https://doi.org/10.1029/2004jb003368).
- Gabriel, A.-A., D. I. Garagash, K. H. Palgunadi & P. M. Mai (2024). "Fault size-dependent fracture energy explains multi-scale seismicity and cascading earthquakes". *Science* 385.6707. DOI: [10.1126/science.adj9587](https://doi.org/10.1126/science.adj9587).
- Gomberg, J., A. Wech, K. Creager, K. Obara & D. Agnew (2016). "Reconsidering earthquake scaling". *Geophysical Research Letters* 43.12, pp. 6243–6251. DOI: [10.1002/2016g1069967](https://doi.org/10.1002/2016g1069967).
- Gounon, A., S. Latour, J. Letort & S. El Arem (2022). "Rupture Nucleation on a Periodically Heterogeneous Interface". *Geophysical Research Letters* 49.20. e2021GL096816. DOI: [10.1029/2021GL096816](https://doi.org/10.1029/2021GL096816).
- Gusev, A. A. (1983). "Descriptive statistical model of earthquake source radiation and its application to an estimation of short-period strong motion". *Geophysical Journal International* 74.3, pp. 787–808. DOI: [10.1111/j.1365-246X.1983.tb01904.x](https://doi.org/10.1111/j.1365-246X.1983.tb01904.x).
- Gutenberg, B. & C. F. Richter (1942). "Earthquake magnitude, intensity, energy, and acceleration". *Bulletin of the Seismological Society of America* 32.3, pp. 163–191. DOI: [10.1785/bssa0320030163](https://doi.org/10.1785/bssa0320030163).
- Hackbusch, W. (1999). "A sparse matrix arithmetic based on-matrices. Part I: Introduction to-matrices". *Computing* 62.2, pp. 89–108. DOI: [10.1007/s006070050015](https://doi.org/10.1007/s006070050015).
- Hanks, T. C. & H. Kanamori (1979). "A moment magnitude scale". *Journal of Geophysical Research: Solid Earth* 84.B5, pp. 2348–2350. DOI: [10.1029/jb084ib05p02348](https://doi.org/10.1029/jb084ib05p02348).
- Hanks, T. C. & R. K. McGuire (1981). "The character of high-frequency strong ground motion". *Bull. Seismol. Soc. Am.* 71.6, pp. 2071–2095. DOI: [10.1785/BSSA0710062071](https://doi.org/10.1785/BSSA0710062071).

- Heimisson, E. R., E. M. Dunham & M. Almquist (2019). "Poroelastic effects destabilize mildly rate-strengthening friction to generate stable slow slip pulses". *Journal of the Mechanics and Physics of Solids* 130, pp. 262–279. DOI: [10.1016/j.jmps.2019.06.007](https://doi.org/10.1016/j.jmps.2019.06.007).
- Hirahara, K, N Mitsui & T Hori (2009). "Development of a fast code for earthquake cycle simulation-(1) Application of Fast Multipole Method". *Eos Trans. AGU* 90(52), Fall Meet. Suppl. Abstract T23C–1929.
- Hirose, H., K. Hirahara, F. Kimata, N. Fujii & S. Miyazaki (1999). "A slow thrust slip event following the two 1996 Hyuganada Earthquakes beneath the Bungo Channel, southwest Japan". *Geophysical Research Letters* 26.21, pp. 3237–3240. DOI: [10.1029/1999g1010999](https://doi.org/10.1029/1999g1010999).
- Houston, H. (2001). "Influence of depth, focal mechanism, and tectonic setting on the shape and duration of earthquake source time functions". *Journal of Geophysical Research: Solid Earth* 106.B6, pp. 11137–11150. DOI: [10.1029/2000jb900468](https://doi.org/10.1029/2000jb900468).
- Ide, S. & G. C. Beroza (2023). "Slow earthquake scaling reconsidered as a boundary between distinct modes of rupture propagation". *Proceedings of the National Academy of Sciences* 120.32. DOI: [10.1073/pnas.2222102120](https://doi.org/10.1073/pnas.2222102120).
- Ide, S., G. C. Beroza, D. R. Shelly & T. Uchide (2007). "A scaling law for slow earthquakes". *Nature* 447.7140, pp. 76–79. DOI: [10.1038/nature05780](https://doi.org/10.1038/nature05780).
- Ide, S., K. Imanishi, Y. Yoshida, G. C. Beroza & D. R. Shelly (2008). "Bridging the gap between seismically and geodetically detected slow earthquakes". *Geophysical Research Letters* 35.10. DOI: [10.1029/2008g1034014](https://doi.org/10.1029/2008g1034014).
- Im, K. & J.-P. Avouac (2023). "Cascading foreshocks, aftershocks and earthquake swarms in a discrete fault network". *Geophysical Journal International* 235.1, pp. 831–852. DOI: [10.1093/gji/ggad278](https://doi.org/10.1093/gji/ggad278).
- Im, K. & J.-P. Avouac (2024). "Quake-DFN: A Software for Simulating Sequences of Induced Earthquakes in a Discrete Fault Network". *Bulletin of the Seismological Society of America* 114.5, pp. 2341–2358. DOI: [10.1785/0120230299](https://doi.org/10.1785/0120230299).
- Ito, Y., R. Hino, M. Kido, H. Fujimoto, Y. Osada, D. Inazu, Y. Ohta, T. Iinuma, M. Ohzono, S. Miura, M. Mishina, K. Suzuki, T. Tsuji & J. Ashi (2013). "Episodic slow slip events in the Japan subduction zone before the 2011 Tohoku-Oki earthquake". *Tectonophysics* 600, pp. 14–26. DOI: [10.1016/j.tecto.2012.08.022](https://doi.org/10.1016/j.tecto.2012.08.022).
- Jara, J., L. Bruhat, M. Y. Thomas, S. L. Antoine, K. Okubo, E. Rougier, A. J. Rosakis, C. G. Sammis, Y. Klinger, R. Jolivet & H. S. Bhat (2021). "Signature of transition to supershear rupture speed in the coseismic off-fault damage zone". *Proceedings of the Royal Society A: Mathematical, Physical and Engineering Sciences* 477.2255. DOI: [10.1098/rspa.2021.0364](https://doi.org/10.1098/rspa.2021.0364).
- Jiang, J., B. A. Erickson, V. R. Lambert, J. Ampuero, R. Ando, S. D. Barbot, C. Cattania, L. D. Zilio, B. Duan, E. M. Dunham, A. Gabriel, N. Lapusta, D. Li, M. Li, D. Liu, Y. Liu, S. Ozawa, C. Pranger & Y. van Dinther (2022). "Community-Driven Code Comparisons for Three-Dimensional Dynamic Modeling of Sequences of Earthquakes and Aseismic Slip". *Journal of Geophysical Research: Solid Earth* 127.3. DOI: [10.1029/2021jb023519](https://doi.org/10.1029/2021jb023519).
- Johnson, K. M., J. Fukuda & P. Segall (2012). "Challenging the rate-state asperity model: Afterslip following the 2011 M9 Tohoku-oki, Japan, earthquake". *Geophysical Research Letters* 39.20. DOI: [10.1029/2012g1052901](https://doi.org/10.1029/2012g1052901).
- Jolivet, R., C. Lasserre, M.-P. Doin, G. Peltzer, J.-P. Avouac, J. Sun & R. Dailu (2013). "Spatio-temporal evolution of aseismic slip along the Haiyuan fault, China: Implications for fault frictional properties". *Earth Planet. Sc. Lett.* 377, pp. 23–33. DOI: [10.1016/j.epsl.2013.07.020](https://doi.org/10.1016/j.epsl.2013.07.020).
- Jones, L. M. & P. Molnar (1979). "Some characteristics of foreshocks and their possible relationship to earthquake prediction and premonitory slip on faults". *Journal of Geophysical Research: Solid Earth* 84.B7, pp. 3596–3608. DOI: [10.1029/jb084ib07p03596](https://doi.org/10.1029/jb084ib07p03596).
- Kame, N., J. R. Rice & R. Dmowska (2003). "Effects of prestress state and rupture velocity on dynamic fault branching". *Journal of Geophysical Research: Solid Earth* 108.B5. DOI: [10.1029/2002jb002189](https://doi.org/10.1029/2002jb002189).
- Kame, N. & T. Yamashita (2003). "Dynamic branching, arresting of rupture and the seismic wave radiation in self-chosen crack path modelling". *Geophysical Journal International* 155.3, pp. 1042–1050. DOI: [10.1111/j.1365-246x.2003.02113.x](https://doi.org/10.1111/j.1365-246x.2003.02113.x).
- Kanamori, H. & D. L. Anderson (1975). "Theoretical basis of some empirical relations in seismology". *Bulletin of the Seismological Society of America* 65.5, pp. 1073–1095. DOI: [10.1785/BSSA0650051073](https://doi.org/10.1785/BSSA0650051073).
- Kanamori, H. & E. E. Brodsky (2001). "The Physics of Earthquakes". *Physics Today* 54.6, pp. 34–40. DOI: [10.1063/1.1387590](https://doi.org/10.1063/1.1387590).
- Kanamori, H. & E. E. Brodsky (2004). "The physics of earthquakes". *Reports on Progress in Physics* 67.8, pp. 1429–1496. DOI: [10.1088/0034-4885/67/8/r03](https://doi.org/10.1088/0034-4885/67/8/r03).
- Kato, A. & Y. Ben-Zion (2020). "The generation of large earthquakes". *Nature Reviews Earth & Environment* 2.1, pp. 26–39. DOI: [10.1038/s43017-020-00108-w](https://doi.org/10.1038/s43017-020-00108-w).
- Kato, N., M. Ohtake & T. Hirasawa (1997). "Possible Mechanism of Precursory Seismic Quiescence: Regional Stress Relaxation due to Preseismic Sliding". *pure and applied geophysics* 150.2, pp. 249–267. DOI: [10.1007/s000240050075](https://doi.org/10.1007/s000240050075).
- King, G. & J. Nábelek (1985). "Role of Fault Bends in the Initiation and Termination of Earthquake Rupture". *Science* 228.4702, pp. 984–987. DOI: [10.1126/science.228.4702.984](https://doi.org/10.1126/science.228.4702.984).

- Klinger, Y., K. Okubo, A. Vallage, J. Champenois, A. Delorme, E. Rougier, Z. Lei, E. E. Knight, A. Munjiza, C. Satriano, S. Baize, R. Langridge & H. S. Bhat (2018). "Earthquake Damage Patterns Resolve Complex Rupture Processes". *Geophysical Research Letters* 45.19. DOI: [10.1029/2018gl1078842](https://doi.org/10.1029/2018gl1078842).
- Kwiatak, G., P. Martínez-Garzón, D. Becker, G. Dresen, F. Cotton, G. C. Beroza, D. Acael, S. Ergintav & M. Bohnhoff (2023). "Months-long seismicity transients preceding the 2023 Mw 7.8 Kahramanmaraş earthquake, Türkiye". *Nature Communications* 14.1. DOI: [10.1038/s41467-023-42419-8](https://doi.org/10.1038/s41467-023-42419-8).
- Lapusta, N. & Y. Liu (2009). "Three-dimensional boundary integral modeling of spontaneous earthquake sequences and aseismic slip". *Journal of Geophysical Research: Solid Earth* 114.B9. DOI: [10.1029/2008jb005934](https://doi.org/10.1029/2008jb005934).
- Lapusta, N., J. R. Rice, Y. Ben-Zion & G. Zheng (2000). "Elastodynamic analysis for slow tectonic loading with spontaneous rupture episodes on faults with rate- and state-dependent friction". *Journal of Geophysical Research: Solid Earth* 105.B10, pp. 23765–23789. DOI: [10.1029/2000jb900250](https://doi.org/10.1029/2000jb900250).
- Lee, J., V. C. Tsai, G. Hirth, A. Chatterjee & D. T. Trugman (2024). "Fault-network geometry influences earthquake frictional behaviour". *Nature* 631.8019, pp. 106–110. DOI: [10.1038/s41586-024-07518-6](https://doi.org/10.1038/s41586-024-07518-6).
- Lee, J.-J. & R. L. Bruhn (1996). "Structural anisotropy of normal fault surfaces". *Journal of Structural Geology* 18.8, pp. 1043–1059. DOI: [10.1016/0191-8141\(96\)00022-3](https://doi.org/10.1016/0191-8141(96)00022-3).
- Leeman, J. R., C. Marone & D. M. Saffer (2018). "Frictional Mechanics of Slow Earthquakes". *Journal of Geophysical Research: Solid Earth* 123.9, pp. 7931–7949. DOI: [10.1029/2018jb015768](https://doi.org/10.1029/2018jb015768).
- Leeman, J. R., D. M. Saffer, M. M. Scuderi & C. Marone (2016). "Laboratory observations of slow earthquakes and the spectrum of tectonic fault slip modes". *Nature Communications* 7.1. DOI: [10.1038/ncomms11104](https://doi.org/10.1038/ncomms11104).
- Li, D. & Y. Liu (2016). "Spatiotemporal evolution of slow slip events in a nonplanar fault model for northern Cascadia subduction zone". *Journal of Geophysical Research: Solid Earth* 121.9, pp. 6828–6845. DOI: [10.1002/2016jb012857](https://doi.org/10.1002/2016jb012857).
- Liu, J., S. Jónsson, X. Li, W. Yao & Y. Klinger (2025). "Extensive off-fault damage around the 2023 Kahramanmaraş earthquake surface ruptures". *Nature Communications* 16.1. DOI: [10.1038/s41467-025-56466-w](https://doi.org/10.1038/s41467-025-56466-w).
- Liu, Y. & J. R. Rice (2005). "Aseismic slip transients emerge spontaneously in three-dimensional rate and state modeling of subduction earthquake sequences". *Journal of Geophysical Research: Solid Earth* 110.B8. DOI: [10.1029/2004jb003424](https://doi.org/10.1029/2004jb003424).
- Liu, Y. & J. R. Rice (2007). "Spontaneous and triggered aseismic deformation transients in a subduction fault model". *Journal of Geophysical Research* 112, B09404. DOI: [10.1029/2007jb004930](https://doi.org/10.1029/2007jb004930).
- Liu, Y. & A. M. Rubin (2010). "Role of fault gouge dilatancy on aseismic deformation transients". *Journal of Geophysical Research: Solid Earth* 115.B10. DOI: [10.1029/2010jb007522](https://doi.org/10.1029/2010jb007522).
- Lowry, A. R., K. M. Larson, V. Kostoglodov & R. Bilham (2001). "Transient fault slip in Guerrero, southern Mexico". *Geophysical Research Letters* 28.19, pp. 3753–3756. DOI: [10.1029/2001gl1013238](https://doi.org/10.1029/2001gl1013238).
- Marone, C. (1998). "Laboratory-derived friction laws and their application to seismic faulting". *Ann. Rev. Earth Planet. Sci.* 26.1, pp. 643–696. DOI: [10.1146/annurev.earth.26.1.643](https://doi.org/10.1146/annurev.earth.26.1.643).
- Marshall, E. & R. Douilly (2024). "Effects of Dip Angle on Rupture Propagation Along Branch Fault Systems". *Bulletin of the Seismological Society of America* 115.1, pp. 54–68. DOI: [10.1785/0120240031](https://doi.org/10.1785/0120240031).
- Marty, S., F. X. Passelègue, J. Aubry, H. S. Bhat, A. Schubnel & R. Madariaga (2019). "Origin of High-Frequency Radiation During Laboratory Earthquakes". *Geophysical Research Letters* 46.7, pp. 3755–3763. DOI: [10.1029/2018gl1080519](https://doi.org/10.1029/2018gl1080519).
- Marty, S., A. Schubnel, H. S. Bhat, J. Aubry, E. Fukuyama, S. Latour, S. Nielsen & R. Madariaga (2023). "Nucleation of Laboratory Earthquakes: Quantitative Analysis and Scalings". *Journal of Geophysical Research: Solid Earth* 128.3. DOI: [10.1029/2022jb026294](https://doi.org/10.1029/2022jb026294).
- Marzocchi, W. & L. Sandri (2009). "A review and new insights on the estimation of the b-value and its uncertainty". *Annals of Geophysics* 46.6. DOI: [10.4401/ag-3472](https://doi.org/10.4401/ag-3472).
- Meier, M.-A., J. P. Ampuero & T. H. Heaton (2017). "The hidden simplicity of subduction megathrust earthquakes". *Science* 357.6357, pp. 1277–1281. DOI: [10.1126/science.aan5643](https://doi.org/10.1126/science.aan5643).
- Meyer, G. G., C. Giorgetti, S. Guérin-Marthe & M. Violay (2024). "Off-fault deformation feedback and strain localization precursor during laboratory earthquakes". *Communications Earth & Environment* 5.1. DOI: [10.1038/s43247-024-01756-2](https://doi.org/10.1038/s43247-024-01756-2).
- Michel, S., J. Avouac, N. Lapusta & J. Jiang (2017). "Pulse-like partial ruptures and high-frequency radiation at creeping-locked transition during megathrust earthquakes". *Geophysical Research Letters* 44.16, pp. 8345–8351. DOI: [10.1002/2017gl1074725](https://doi.org/10.1002/2017gl1074725).
- Michel, S., A. Gualandi & J.-P. Avouac (2019). "Similar scaling laws for earthquakes and Cascadia slow-slip events". *Nature* 574.7779, pp. 522–526. DOI: [10.1038/s41586-019-1673-6](https://doi.org/10.1038/s41586-019-1673-6).
- Milliner, C., J. P. Avouac, J. F. Dolan & J. Hollingsworth (2025). "Localization of inelastic strain with fault maturity and effects on earthquake characteristics". *Nature Geoscience*. DOI: [10.1038/s41561-025-01752-x](https://doi.org/10.1038/s41561-025-01752-x).
- Mitchell, T. & D. Faulkner (2009). "The nature and origin of off-fault damage surrounding strike-slip fault zones with a wide range of displacements: A field study from the Atacama fault system, northern Chile". *Journal of Structural Geology* 31.8, pp. 802–816. DOI: [10.1016/j.jsg.2009.05.002](https://doi.org/10.1016/j.jsg.2009.05.002).

- Nevitt, J. M., B. A. Brooks, J. L. Hardebeck & B. T. Aagaard (2023). "2019 M7.1 Ridgecrest earthquake slip distribution controlled by fault geometry inherited from Independence dike swarm". *Nature Communications* 14.1. DOI: [10.1038/s41467-023-36840-2](https://doi.org/10.1038/s41467-023-36840-2).
- Nie, S. & S. Barbot (2021). "Seismogenic and tremorgenic slow slip near the stability transition of frictional sliding". *Earth and Planetary Science Letters* 569, p. 117037. DOI: [10.1016/j.epsl.2021.117037](https://doi.org/10.1016/j.epsl.2021.117037).
- Niemeijer, A., C. Marone & D. Elsworth (2010). "Fabric induced weakness of tectonic faults". *Geophysical Research Letters* 37.3. DOI: [10.1029/2009GL041689](https://doi.org/10.1029/2009GL041689).
- Nishikawa, T., S. Ide & T. Nishimura (2023). "A review on slow earthquakes in the Japan Trench". *Progress in Earth and Planetary Science* 10.1. DOI: [10.1186/s40645-022-00528-w](https://doi.org/10.1186/s40645-022-00528-w).
- Núñez-Jara, S., P. Martínez-Garzón, G. Kwiatek, Y. Ben-Zion, G. Dresen, D. Becker, F. Cotton & M. Bohnhoff (2025). "Unraveling the spatiotemporal fault activation in a complex fault system: the run-up to the 2023 MW 7.8 Kahramanmaraş earthquake, Türkiye". *Earth and Planetary Science Letters* 669, p. 119570. DOI: [10.1016/j.epsl.2025.119570](https://doi.org/10.1016/j.epsl.2025.119570).
- Nur, A. (1978). "Nonuniform friction as a physical basis for earthquake mechanics". *pure and applied geophysics* 116.4–5, pp. 964–989. DOI: [10.1007/BF00876550](https://doi.org/10.1007/BF00876550).
- Obara, K. (2002). "Nonvolcanic Deep Tremor Associated with Subduction in Southwest Japan". *Science* 296.5573, pp. 1679–1681. DOI: [10.1126/science.1070378](https://doi.org/10.1126/science.1070378).
- Obara, K. & A. Kato (2016). "Connecting slow earthquakes to huge earthquakes". *Science* 353.6296, pp. 253–257. DOI: [10.1126/science.aaf1512](https://doi.org/10.1126/science.aaf1512).
- Oglesby, D. D. (2003). "The 1999 Hector Mine Earthquake: The Dynamics of a Branched Fault System". *Bulletin of the Seismological Society of America* 93.6, pp. 2459–2476. DOI: [10.1785/0120030026](https://doi.org/10.1785/0120030026).
- Oglesby, D. D. (2005). "The Dynamics of Strike-Slip Step-Overs with Linking Dip-Slip Faults". *Bulletin of the Seismological Society of America* 95.5, pp. 1604–1622. DOI: [10.1785/0120050058](https://doi.org/10.1785/0120050058).
- Ohnaka, M. (2003). "A constitutive scaling law and a unified comprehension for frictional slip failure, shear fracture of intact rock, and earthquake rupture". *Journal of Geophysical Research: Solid Earth* 108.B2. DOI: [10.1029/2000jb000123](https://doi.org/10.1029/2000jb000123).
- Ohnaka, M. & L.-f. Shen (1999). "Scaling of the shear rupture process from nucleation to dynamic propagation: Implications of geometric irregularity of the rupturing surfaces". *J. Geophys. Res.* 104.B1, pp. 817–844. DOI: [10.1029/1998JB900007](https://doi.org/10.1029/1998JB900007).
- Okubo, K., H. S. Bhat, E. Rougier, S. Marty, A. Schubnel, Z. Lei, E. E. Knight & Y. Klinger (2019). "Dynamics, Radiation, and Overall Energy Budget of Earthquake Rupture With Coseismic Off-Fault Damage". *Journal of Geophysical Research: Solid Earth* 124.11, pp. 11771–11801. DOI: [10.1029/2019jb017304](https://doi.org/10.1029/2019jb017304).
- Okubo, K., E. Rougier, Z. Lei & H. S. Bhat (2020). "Modeling earthquakes with off-fault damage using the combined finite-discrete element method". *Computational Particle Mechanics* 7.5, pp. 1057–1072. DOI: [10.1007/s40571-020-00335-4](https://doi.org/10.1007/s40571-020-00335-4).
- Omori, F. (1894). "On after-shocks of earthquakes". *J. Coll. Sci. Imp. Univ. Tokyo* 7, pp. 111–200.
- Ostermeijer, G. A., T. M. Mitchell, F. M. Aben, M. T. Dorsey, J. Browning, T. K. Rockwell, J. M. Fletcher & F. Ostermeijer (2020). "Damage zone heterogeneity on seismogenic faults in crystalline rock; a field study of the Borrego Fault, Baja California". *Journal of Structural Geology* 137, p. 104016. DOI: [10.1016/j.jsg.2020.104016](https://doi.org/10.1016/j.jsg.2020.104016).
- Ozawa, S. & R. Ando (2021). "Mainshock and Aftershock Sequence Simulation in Geometrically Complex Fault Zones". *Journal of Geophysical Research: Solid Earth* 126.2. DOI: [10.1029/2020jb020865](https://doi.org/10.1029/2020jb020865).
- Ozawa, S., R. Ando & E. M. Dunham (2023). "Quantifying the probability of rupture arrest at restraining and releasing bends using earthquake sequence simulations". *Earth and Planetary Science Letters* 617, p. 118276. DOI: [10.1016/j.epsl.2023.118276](https://doi.org/10.1016/j.epsl.2023.118276).
- Ozawa, S., Y. Yang & E. M. Dunham (2024). "Fault-Valve Instability: A Mechanism for Slow Slip Events". *Journal of Geophysical Research: Solid Earth* 129.10. DOI: [10.22541/essoar.171291623.31088922/v1](https://doi.org/10.22541/essoar.171291623.31088922/v1).
- Papazachos, B. C. (1973). "The time distribution of the reservoir-associated foreshocks and its importance to the prediction of the principal shock". *Bulletin of the Seismological Society of America* 63.6–1, pp. 1973–1978. DOI: [10.1785/bssa0636-11973](https://doi.org/10.1785/bssa0636-11973).
- Perez-Silva, A., Y. Kaneko, M. Savage, L. Wallace & E. Warren-Smith (2023). "Characteristics of Slow Slip Events Explained by Rate-Strengthening Faults Subject to Periodic Pore Fluid Pressure Changes". *Journal of Geophysical Research: Solid Earth* 128.6. DOI: [10.22541/essoar.167327976.60438163/v1](https://doi.org/10.22541/essoar.167327976.60438163/v1).
- Perfettini, H., J. Schmittbuhl, J. R. Rice & M. Cocco (2001). "Frictional response induced by time-dependent fluctuations of the normal loading". *Journal of Geophysical Research* 106.B7, pp. 13455–13472. DOI: [10.1029/2000jb900366](https://doi.org/10.1029/2000jb900366).
- Perrin, C., I. Manighetti & Y. Gaudemer (2015). "Off-fault tip splay networks: A genetic and generic property of faults indicative of their long-term propagation". *Comptes Rendus. Géoscience* 348.1, pp. 52–60. DOI: [10.1016/j.crte.2015.05.002](https://doi.org/10.1016/j.crte.2015.05.002).
- Pignatelli, F., C. Giorgetti, C. Noël, C. Marone, C. Collettini & M. M. Scuderi (2024). "The Effect of Normal Stress Oscillations on Fault Slip Behavior Near the Stability Transition From Stable to Unstable Motion". *Journal of Geophysical Research: Solid Earth* 129.2. DOI: [10.1029/2023jb027470](https://doi.org/10.1029/2023jb027470).
- Power, W. L., T. E. Tullis, S. R. Brown, G. N. Boitnott & C. H. Scholz (1987). "Roughness of natural fault surfaces". *Geophysical Research Letters* 14.1, pp. 29–32. DOI: [10.1029/g1014i001p00029](https://doi.org/10.1029/g1014i001p00029).

- Powers, P. M. & T. H. Jordan (2010). "Distribution of seismicity across strike-slip faults in California". *Journal of Geophysical Research: Solid Earth* 115.B5. DOI: [10.1029/2008jb006234](#).
- Pritchard, M. E., R. M. Allen, T. W. Becker, M. D. Behn, E. E. Brodsky, R. Bürgmann, C. Ebinger, J. T. Freymueller, M. Gerstenberger, B. Haines, Y. Kaneko, S. D. Jacobsen, N. Lindsey, J. J. McGuire, M. Page, S. Ruiz, M. Tolstoy, L. Wallace, W. R. Walter, W. Wilcock & H. Vincent (2020). "New Opportunities to Study Earthquake Precursors". *Seismological Research Letters* 91.5, pp. 2444–2447. DOI: [10.1785/0220200089](#).
- Renard, F., C. Voisin, D. Marsan & J. Schmittbuhl (2006). "High resolution 3D laser scanner measurements of a strike-slip fault quantify its morphological anisotropy at all scales". *Geophysical Research Letters* 33.4. DOI: [10.1029/2005gl025038](#).
- Rice, J. R. (1992). "Fault Stress States, Pore Pressure Distributions, and the Weakness of the San Andreas Fault". *Fault Mechanics and Transport Properties in Rocks*. Ed. by B. Evans & T. F. Wong. Academic Press, pp. 475–503. DOI: [10.1016/S0074-6142\(08\)62835-1](#).
- Rice, J. R. (1993). "Spatio-temporal complexity of slip on a fault". *Journal of Geophysical Research: Solid Earth* 98.B6, pp. 9885–9907. DOI: [10.1029/93jb00191](#).
- Ritz, E., D. D. Pollard & M. Ferris (2015). "The influence of fault geometry on small strike-slip fault mechanics". *Journal of Structural Geology* 73, pp. 49–63. DOI: [10.1016/j.jsg.2014.12.007](#).
- Rodriguez Padilla, A. M., M. E. Oskin, E. E. Brodsky, K. Dascher-Cousineau, V. Herrera & S. White (2024). "The Influence of Fault Geometrical Complexity on Surface Rupture Length". *Geophysical Research Letters* 51.20. DOI: [10.1029/2024gl109957](#).
- Rodriguez Padilla, A. M., M. E. Oskin, C. W. D. Milliner & A. Plesch (2022). "Accrual of widespread rock damage from the 2019 Ridgecrest earthquakes". *Nature Geoscience* 15.3, pp. 222–226. DOI: [10.1038/s41561-021-00888-w](#).
- Rogers, G. & H. Dragert (2003). "Episodic Tremor and Slip on the Cascadia Subduction Zone: The Chatter of Silent Slip". *Science* 300.5627, pp. 1942–1943. DOI: [10.1126/science.1084783](#).
- Romanet, P. (2017). "Fast algorithms to model quasi-dynamic earthquake cycles in complex fault networks". PhD thesis. Institut de Physique du Globe de Paris.
- Romanet, P., H. S. Bhat, R. Jolivet & R. Madariaga (2018). "Fast and Slow Slip Events Emerge Due to Fault Geometrical Complexity". *Geophysical Research Letters* 45.10, pp. 4809–4819. DOI: [10.1029/2018gl1077579](#).
- Romanet, P., T. Saito & E. Fukuyama (2024). "The mechanics of static non-planar faults in infinitesimal strain theory". *Geophys. J. Int.*, gga337. DOI: [10.1093/gji/ggae337](#).
- Romanet, P., D. S. Sato & R. Ando (2020). "Curvature, a mechanical link between the geometrical complexities of a fault: application to bends, kinks and rough faults". *Geophysical Journal International* 223.1, pp. 211–232. DOI: [10.1093/gji/ggaa308](#).
- Rosenfeld, A. & J. L. Pfaltz (1966). "Sequential operations in digital picture processing". *Journal of the ACM (JACM)* 13.4, pp. 471–494. DOI: [10.1145/321356.321357](#).
- Rousset, B., R. Jolivet, M. Simons, C. Lasserre, B. Riel, P. Milillo, Z. Çakir & F. Renard (2016). "An aseismic slip transient on the North Anatolian Fault". *Geophys. Res. Lett.* 43.7, pp. 3254–3262. DOI: [10.1002/2016GL068250](#).
- Rubin, A. M. & J. Ampuero (2005). "Earthquake nucleation on (aging) rate and state faults". *Journal of Geophysical Research: Solid Earth* 110.B11. DOI: [10.1029/2005jb003686](#).
- Rubin, A. M. (2008). "Episodic slow slip events and rate-and-state friction". *Journal of Geophysical Research* 113, B11414. DOI: [10.1029/2008jb005642](#).
- Ruina, A. (1983). "Slip instability and state variable friction laws". *Journal of Geophysical Research: Solid Earth* 88.B12, pp. 10359–10370. DOI: [10.1029/jb088ib12p10359](#).
- Ruiz, S., F. Aden-Antoniow, J. C. Baez, C. Otárola, B. Potin, F. del Campo, P. Poli, C. Flores, C. Satriano, F. Leyton, R. Madariaga & P. Bernard (2017). "Nucleation Phase and Dynamic Inversion of the Mw 6.9 Valparaíso 2017 Earthquake in Central Chile". *Geophysical Research Letters* 44.20. DOI: [10.1002/2017GL075675](#).
- Ruiz, S., M. Metois, A. Fuenzalida, J. Ruiz, F. Leyton, R. Grandin, C. Vigny, R. Madariaga & J. Campos (2014). "Intense foreshocks and a slow slip event preceded the 2014 Iquique M_w 8.1 earthquake". *Science* 345.6201, pp. 1165–1169. DOI: [10.1126/science.1256074](#).
- Salazar Vásquez, A. F., P. A. Selvadurai, P. Bianchi, C. Madonna, L. N. Germanovich, A. M. Puzrin, S. Wiemer, D. Giardini & C. Rabaiotti (2024). "Aseismic strain localization prior to failure and associated seismicity in crystalline rock". *Scientific Reports* 14.1. DOI: [10.1038/s41598-024-75942-9](#).
- Savage, H. M. & E. E. Brodsky (2011). "Collateral damage: Evolution with displacement of fracture distribution and secondary fault strands in fault damage zones". *Journal of Geophysical Research* 116.B3. DOI: [10.1029/2010jb007665](#).
- Schmittbuhl, J., S. Gentier & S. Roux (1993). "Field measurements of the roughness of fault surfaces". *Geophysical Research Letters* 20.8, pp. 639–641. DOI: [10.1029/93gl100170](#).
- Scholz, C. H. (2019). *The mechanics of earthquakes and faulting*. Cambridge Univ Press.
- Schwartz, S. Y. & J. M. Rokyosky (2007). "Slow slip events and seismic tremor at circum-Pacific subduction zones". *Reviews of Geophysics* 45.3. DOI: [10.1029/2006rg000208](#).
- Scuderi, M. M., C. Marone, E. Tinti, G. Di Stefano & C. Collettini (2016). "Precursory changes in seismic velocity for the spectrum of earthquake failure modes". *Nature Geoscience* 9.9, pp. 695–700. DOI: [10.1038/ngeo2775](#).

- Scuderi, M., C. Collettini, C. Viti, E. Tinti & C. Marone (2017). "Evolution of shear fabric in granular fault gouge from stable sliding to stick slip and implications for fault slip mode". *Geology*, G39033.1. DOI: [10.1130/g39033.1](https://doi.org/10.1130/g39033.1).
- Segall, P. & J. R. Rice (1995). "Dilatancy, compaction, and slip instability of a fluid-infiltrated fault". *Journal of Geophysical Research* 100.B11, pp. 22155–22171. DOI: [10.1029/95jb02403](https://doi.org/10.1029/95jb02403).
- Segall, P. & A. M. Bradley (2012). "Slow-slip evolves into megathrust earthquakes in 2D numerical simulations". *Geophysical Research Letters* 39.18. DOI: [10.1029/2012gl052811](https://doi.org/10.1029/2012gl052811).
- Segall, P., A. M. Rubin, A. M. Bradley & J. R. Rice (2010). "Dilatant strengthening as a mechanism for slow slip events". *Journal of Geophysical Research: Solid Earth* 115.B12. DOI: [10.1029/2010jb007449](https://doi.org/10.1029/2010jb007449).
- Shapiro, L. G. & G. C. Stockman (2001). *Computer Vision*. Prentice Hall.
- Shearer, P. M., H. Meng & W. Fan (2023). "Earthquake Detection Using a Nodal Array on the San Jacinto Fault in California: Evidence for High Foreshock Rates Preceding Many Events". *Journal of Geophysical Research: Solid Earth* 128.3. DOI: [10.1029/2022jb025279](https://doi.org/10.1029/2022jb025279).
- Shelly, D. R. (2017). "A 15 year catalog of more than 1 million low-frequency earthquakes: Tracking tremor and slip along the deep San Andreas Fault". *Journal of Geophysical Research: Solid Earth* 122.5, pp. 3739–3753. DOI: [10.1002/2017jb014047](https://doi.org/10.1002/2017jb014047).
- Sibson, R. H. (1977). "Fault rocks and fault mechanisms". *Journal of the Geological Society (London, United Kingdom)* 133.3, pp. 191–213. DOI: [10.1144/gsjgs.133.3.0191](https://doi.org/10.1144/gsjgs.133.3.0191).
- Sibson, R. H. (1986). "Rupture interaction with fault jogs". *Earthquake Source Mechanics*. Ed. by S. Das, J. Boatwright & C. H. Scholz. AGU Geophys. Monogr., pp. 157–167. DOI: [10.1029/gm037p0157](https://doi.org/10.1029/gm037p0157).
- Sibson, R. H. (2003). "Thickness of the Seismic Slip Zone". *Bulletin of the Seismological Society of America* 93.3, pp. 1169–1178. DOI: [10.1785/0120020061](https://doi.org/10.1785/0120020061).
- Sirorattanakul, K. (2024). "Response of Earthquakes to Transient Stresses, in Laboratory and Nature". en. PhD thesis. DOI: [10.7907/2FGG-0M89](https://doi.org/10.7907/2FGG-0M89).
- Skarbek, R. M. & A. W. Rempel (2016). "Dehydration-induced porosity waves and episodic tremor and slip". *Geochemistry, Geophysics, Geosystems* 17.2, pp. 442–469. DOI: [10.1002/2015gc006155](https://doi.org/10.1002/2015gc006155).
- Sowers, J. M., J. R. Unruh, W. R. Lettis & T. D. Rubin (1994). "Relationship of the kickapoo fault to the Johnson Valley and Homestead Valley faults, San Bernardino County, California". *Bulletin of the Seismological Society of America* 84.3, pp. 528–536. DOI: [10.1785/bssa0840030528](https://doi.org/10.1785/bssa0840030528).
- Stein, R. S. & P. Bird (2024). "Why Do Great Continental Transform Earthquakes Nucleate on Branch Faults?" *Seismological Research Letters*. DOI: [10.1785/0220240175](https://doi.org/10.1785/0220240175).
- Steinbrugge, K. V., E. G. Zacher, D. Tocher, C. Whitten & C. Claire (1960). "Creep on the San Andreas fault". *Bulletin of The Seismological Society of America* 50.3, pp. 389–415. DOI: [10.1785/bssa0500030389](https://doi.org/10.1785/bssa0500030389).
- Tada, T. & T. Yamashita (1997). "Non-hypersingular boundary integral equations for two-dimensional non-planar crack analysis". *Geophysical Journal International* 130.2, pp. 269–282. DOI: [10.1111/j.1365-246x.1997.tb05647.x](https://doi.org/10.1111/j.1365-246x.1997.tb05647.x).
- The MathWorks, Inc. (2024). *Image Processing Toolbox*. Available at: <https://www.mathworks.com/help/images/ref/bwlabel.html>. Natick, Massachusetts, United States.
- Thomas, M. Y., J.-P. Avouac, J.-P. Gratier & J.-C. Lee (2014). "Lithological control on the deformation mechanism and the mode of fault slip on the Longitudinal Valley Fault, Taiwan". *Tectonophysics* 632, pp. 48–63. DOI: [10.1016/j.tecto.2014.05.038](https://doi.org/10.1016/j.tecto.2014.05.038).
- Thomas, M. Y., J.-P. Avouac & N. Lapusta (2017). "Rate-and-state friction properties of the Longitudinal Valley Fault from kinematic and dynamic modeling of seismic and aseismic slip". *Journal of Geophysical Research-solid Earth* 122, pp. 3115–3137. DOI: <https://doi.org/10.1002/2016JB013615>.
- Thomas, M. Y. & H. S. Bhat (2018). "Dynamic evolution of off-fault medium during an earthquake: a micromechanics based model". *Geophysical Journal International* 214.2, pp. 1267–1280. DOI: [10.1093/gji/ggy129](https://doi.org/10.1093/gji/ggy129).
- Tinti, E., M. M. Scuderi, L. Scognamiglio, G. Di Stefano, C. Marone & C. Collettini (2016). "On the evolution of elastic properties during laboratory stick-slip experiments spanning the transition from slow slip to dynamic rupture". *Journal of Geophysical Research: Solid Earth* 121.12, pp. 8569–8594. DOI: [10.1002/2016jb013545](https://doi.org/10.1002/2016jb013545).
- Utsu, T., Y. Ogata, R. S. & Matsu'ura (1995). "The Centenary of the Omori Formula for a Decay Law of Aftershock Activity". *Journal of Physics of the Earth* 43.1, pp. 1–33. DOI: [10.4294/jpe1952.43.1](https://doi.org/10.4294/jpe1952.43.1).
- Vallée, M., J. Nocquet, J. Battaglia, Y. Font, M. Segovia, M. Régnier, P. Mothes, P. Jarrin, D. Cisneros, S. Vaca, H. Yepes, X. Martin, N. Béthoux & M. Chlieh (2013). "Intense interface seismicity triggered by a shallow slow slip event in the Central Ecuador subduction zone". *Journal of Geophysical Research: Solid Earth* 118.6, pp. 2965–2981. DOI: [10.1002/jgrb.50216](https://doi.org/10.1002/jgrb.50216).
- Viesca, R. C. (2016). "Stable and unstable development of an interfacial sliding instability". *Physical Review E: Statistical Physics, Plasmas, Fluids, and Related Interdisciplinary Topics* 93.6, p. 060202. DOI: [10.1103/PhysRevE.93.060202](https://doi.org/10.1103/PhysRevE.93.060202).
- Villafuerte, C., V. M. Cruz-Atienza, J. Tago, D. Solano-Rojas, R. Garza-Girón, S. I. Franco, L. A. Domínguez & V. Kostoglodov (2025). "Slow slip events and megathrust coupling changes contribute to the earthquake potential in Oaxaca, Mexico". *Geophysical Journal International* 241.1, pp. 17–34. DOI: [10.5194/egusphere-egu25-15266](https://doi.org/10.5194/egusphere-egu25-15266).

- Walt, S. van der, J. L. Schönberger, J. Nunez-Iglesias, F. Boulogne, J. D. Warner, N. Yager, E. Gouillart & T. Yu (2014). "scikit-image: Image processing in Python". *PeerJ* 2, e453. DOI: [10.7717/peerj.453](https://doi.org/10.7717/peerj.453).
- Wang, Q.-Y., W. B. Frank, R. E. Abercrombie, K. Obara & A. Kato (2023a). "What makes low-frequency earthquakes low frequency". *Science Advances* 9.32. DOI: [10.5194/egusphere-egu23-9067](https://doi.org/10.5194/egusphere-egu23-9067).
- Wang, X., L. Dal Zilio, J. K. Morgan & D. S. Kammer (2023b). "Non-Precursory Accelerating Aseismic Slip During Rupture Nucleation". *Journal of Geophysical Research: Solid Earth* 128.6. DOI: [10.1029/2022jb026066](https://doi.org/10.1029/2022jb026066).
- Yabe, S. & K. Ujiie (2025). "Tectonic Tremor Explained by Successive Ruptures of Clustered Quartz-Filled Shear Veins". *Geophysical Research Letters* 52.14. DOI: [10.1029/2025gl115447](https://doi.org/10.1029/2025gl115447).
- Yin, Y., P. Galvez, E. R. Heimissson & S. Wiemer (2023). "The role of three-dimensional fault interactions in creating complex seismic sequences". *Earth and Planetary Science Letters* 606, p. 118056. DOI: [10.1016/j.epsl.2023.118056](https://doi.org/10.1016/j.epsl.2023.118056).
- Yoshida, S. & N. Kato (2003). "Episodic aseismic slip in a two-degree-of-freedom block-spring model". *Geophysical Research Letters* 30.13. DOI: [10.1029/2003GL017439](https://doi.org/10.1029/2003GL017439).
- Yuan, C., T. Cochard, M. Denolle, J. Gomberg, A. Wech, L. Xiao & D. Weitz (2024). "Laboratory Hydrofractures as Analogs to Tectonic Tremors". *AGU Advances* 5.1. DOI: [10.1029/2023av001002](https://doi.org/10.1029/2023av001002).
- Zhu, W., K. L. Allison, E. M. Dunham & Y. Yang (2020). "Fault valving and pore pressure evolution in simulations of earthquake sequences and aseismic slip". *Nature Communications* 11.1. DOI: [10.1038/s41467-020-18598-z](https://doi.org/10.1038/s41467-020-18598-z).